Ultrasound Elastography: Direct Strain Estimation

Hossein Khodadadi

A Thesis

in

The Department

of

Electrical and Computer Engineering

Presented in Partial Fulfillment of the Requirements

for the Degree of Master of Applied Science at

Concordia University

Montréal, Québec, Canada

September 2017

CONCORDIA UNIVERSITY

SCHOOL OF GRADUATE STUDIES

This is to certify that the thesis prepared

By: Hossein Khodadadi

Entitled: Ultrasound Elastography: Direct Strain Estimation

and submitted in partial fulfilment of the requirements for the degree of

Master of Applied Science

Complies with the regulations of this University and meets the accepted standards

with respect to originality and quality.

Signed by the final examining committee:

————————————————————— Dr. Rabin Raut, Chair

————————————————————— Dr. Ramin Sedaghati, External Examiner

————————————————————— Dr. Steve Shih, Examiner

————————————————————— Dr. Hassan Rivaz, Supervisor

————————————————————— Dr. A. G. Aghdam, Supervisor

Approved by: ——————————————————————————————

     Dr. William E. Lynch, Chair

       Department of Electrical and Computer Engineering

————————— 20 —————————————————————————

        Dr. Amir Asif

      Dean, Faculty of Engineering and Computer Science

ABSTRACT

Ultrasound Elastography: Direct Strain Estimation

Hossein Khodadadi

Ultrasound elastography involves measuring the mechanical properties of tissue, and has many applications in diagnostics and intervention. Ultrasound elastography techniques mainly target obtaining strain images from raw Radio-Frequency (RF) echo field produced by ultrasound machine without adding any hardware. A common step in different elastography methods is imaging the tissue while it undergoes deformation and estimating the displacement field from the images. A popular next step is to estimate tissue strain, which gives clues into the underlying tissue elasticity modulus. To estimate the strain, one should compute the gradient of the displacement image, which amplifies the noise. The noise is commonly minimized by least square estimation of the gradient from multiple displacement measurements, which reduces the noise by sacrificing image resolution.

The first part of this thesis propose a new method which adaptively adjusts the level and orientation of the smoothing strain images using two different mechanisms. First, the precision of the displacement field decreases significantly in the regions with high signal decorrelation, which requires increasing the smoothness. Second, smoothing the strain field at the boundaries between different tissue types blurs the edges, which can render small targets invisible. To minimize blurring and noise, we perform anisotropic smoothing and perform smoothing parallel to the direction of

the edges. The first mechanism ensures that textures/variations in the strain image reflect underlying tissue properties and are not caused by errors in the displacement estimation. The second mechanism keeps the edges between different tissue structures sharp while minimizing the noise.

The second part of this thesis introduces a 2D strain imaging technique called SHORT-CUT (meSHing Of gRadienT in DP for direCt Ultrasound elasTography) based on minimizing a cost function. The cost function incorporates similarity of echo amplitudes and tissue continuity. The proposed technique is fast, robust and accurate and it directly produces the strain images from RF data using a novel dynamic programming (DP) configuration. Unlike the standard DP algorithm which discretizes the decision space (displacement field) and search in the space of piecewise constant functions, the proposed DP discretizes the gradient of the decision space (strain field) and search the space of continuous piecewise linear functions. Eliminating the displacement differentiation block and performing a global search instead of local search which exist in all of the available strain estimation techniques result in substantial improvement in SNR, CNR and accuracy of the estimations. The effectiveness of the proposed methods is investigated through simulation data, phantom experiments, and *in vivo* patient data.

To my beloved parents

ACKNOWLEDGEMENTS

My appreciation, first and foremost goes to my knowledgeable, erudite and exceptional supervisors, Prof. Amir G. Aghdam and Prof. Hassan Rivaz for their kind supports and patient guidances. Their encouragements, motivation and immense knowledge, were the invaluable assets I had throughout my experience in this research study and I am deeply grateful for them.

Also, I do appreciate my friend and colleague in Concordia University, Mr. Mohammad Khosravi, for his patience and kindness in our collaborations. I was very fortunate to have the most rewarding discussions with him.

I ultimately would like to thank my beloved dad, mom and sisters for their love and warm support.

TABLE OF CONTENTS

LIST OF TABLES

LIST OF FIGURES

Chapter 1

Introduction

Acoustic waves with frequencies above 20 kHz are considered as ultrasound. Medical ultrasound machines typically use a frequency range of 1 MHz to 10 MHz. Since medical ultrasound is non-ionizing, inexpensive, real-time and easy to use, it is the preferred modality in many diagnostic and surgical procedures in both equipped and unequipped clinics and hospitals. A probe which consists of an array of small piezo-electric transducers is responsible for both triggering and sensing acoustic waves. The probe is placed on the surface of the skin and triggers the skin with acoustic waves. A short ultrasound pulse is transmitted by the probe into the tissue where a portion of it is reflected from numerous interfaces between tissue types with different acoustic properties. The reflected waves (echoes) travel back to the piezoelectric crystals and are converted to electrical voltages by the same piezoelectric effect. This unprocessed electrical signal is called the Radio-Frequency (RF) signal. By measuring the envelope of these RF signals and converting them to brightness, the B-mode image is produced

which is the main visual output of ultrasound machines. Given the propagation speed of sound, the depth of a tissue boundary can be calculated by measuring the transit time from the initial pulse transmission to reception of the echo. The amplitude of the echo represents the relative difference of acoustical properties at the boundary. The back-scattered echoes from the resolution cell, which is an approximately ellipsoidal area, forms the pixels in an ultrasound image. Speckles [1], which are responsible for the grainy appearance of the ultrasound image, are created by the interference of scatterers in a resolution cell. In spite of their random appearance, the speckle patterns are reproducible in the sense that they remain identical if the same object is scanned again under the same conditions (same direction, frequency and focusing). This property opens a new horizon for extracting more information (e.g., about the mechanical properties of the tissue) from the raw RF data.

Ultrasound elastography is an emerging field of research which aims to reveal the mechanical properties of tissue and has numerous applications in both diagnostics and surgical planning [2–8]. Numerous techniques have been used in ultrasound elastography which can be predominantly categorized into dynamic and quasi-static elastography. In quasi-static elastography, the tissue is deformed slowly and displacement field is estimated using the pre and post-deformed ultrasound RF data. Differentiating the displacement field produces the strain image. They can also be used in an inverse problem formulation to calculate tissue elasticity modulus [9, 10]. In dynamic elastography, on the other hand, a quantitative measure of the mechanical

properties of the tissue is obtained by following the acoustic wave propagation using ultrasound. Dynamic elastography uses the wave equation of shear waves and hence, do not need to know the stress distribution to estimate the local Young's modulus. However, since both compression and shear waves are present in the studied medium and the waves rebound at the interfaces and are mixed together, it's very difficult to distinguish them. Therefore, the quality of estimations in dynamic elastography is low and it's very sensitive to the boundary conditions. More comprehensive surveys on dynamic elastography can be found in [4, 11]. Exploiting the fact that shear waves are three times slower than compression waves and using transient excitation, transient elastography was developed to overcome these limitation by separating shear waves from compression waves. Acoustic Radiation Force Impulse Imaging (ARFI) [12] is a transient elastography method which uses the acoustic radiation force in the form of one focalized ultrasound beam. The radiation force slightly displaces the tissue and, similar to quasi-static elastography, the displacement field is estimated. Following the displacement and the relaxation of tissue depending on the radiation force allow the deduction of elasticity and viscosity at the focal spot only [13]. The disadvantages of ARFI are the deposited energy in the medium which can cause consequent heating [14, 15] and the fact that it cannot be used to quantitatively estimate tissue Young's modulus although the measured parameters strongly depend on it.

This thesis investigated some important problems in quasi-static elastography, with a special focus on free-hand palpation elastography. Unlike dynamic elastography (unless it is combined with an inverse problem approach [9, 10]), quasi-static

elastography cannot compute the tissue elasticity modulus. However, since they can estimate larger displacement fields compared to that of shear-wave elastography, they may produce strain images with better Signal-to-Noise Ratio (SNR) and Contrast-To-Noise ratio (CNR) and they need no equipment and technology other than traditional ultrasound machines. Various methods have been proposed for displacement estimation from RF data, commonly referred to as Time-Delay Estimation (TDE). The most widely used TDE techniques are window-based methods, where RF data is divided into several small windows (segments) and the displacement of each window is estimated using either phased-based [16] or amplitude-based [17–20] techniques. The amplitude-based techniques maximize Cross Correlation (CC) or Normalized Cross Correlation (NCC) of the two corresponding pre and post-deformed windows to compute the tissue displacement. On the contrary, in the phased-based approaches, the phase information of the RF data is used for displacement estimation. Window-based methods are very sensitive to signal decorrelation and need to compromise between better spatial resolution with small windows and higher accuracy with larger windows.

Formulating the TDE as an optimization problem is a popular alternative method for computing the tissue displacement [7, 16, 18, 21–24]. These methods exploit the prior information of motion continuity in tissues, and therefore are robust to signal decorrelation. In [7, 21] a dynamic programming analytical minimization (DPAM) technique is proposed which consists of a cost function that incorporates

4

both similarity of RF echo amplitudes and the prior information of displacement continuity. Using this cost function, DPAM estimates 2D displacement field, and after applying a spatial derivative operator to the displacement field, the strain image is computed. Estimating the strain by performing spatial derivative of the displacement field amplifies the noise. Thus, a least-squares estimation of the strain is commonly performed, which reduces the spatial resolution. At the end, the resulting strain images are smoothed laterally by a Kalman filter.

As mentioned in the previous paragraph, the strain image is obtained by taking spatial derivative of the displacement field and taking derivative amplifies the noise. To overcome this challenge, in the first part of this thesis we propose a new method which adaptively adjusts the level and orientation of the smoothing in strain images using two different mechanisms. The precision of the displacement field decreases significantly in the regions with high signal decorrelation, which requires increasing the smoothness. The first mechanism aims at producing uniform precision strain images by adjusting the level of smoothness. Smoothing the strain field at the boundaries between different tissue types blurs the edges, which can render small targets invisible. The second mechanism minimizes blurring and noise by performing anisotropic smoothing parallel to the direction of edges. The first mechanism ensures that textures/variations in the strain image reflect underlying tissue properties and are not caused by errors in the displacement estimation. The second mechanism keeps the

edges between different tissue structures sharp while minimizing the noise. We validate the proposed method using phantom and *in-vivo* clinical data.

All of the aforementioned methods, including our proposed method in the previous paragraph, follow a pipeline paradigm that consists of displacement estimation followed by strain estimation and a smoothing filter. Aside from amplifying the noise by taking the derivative of the displacement field, the other disadvantage of these pipeline methods is that they do not exploit the information of the RF data in the strain estimation step, and utilize only the noisy displacement field to calculate the strain. The authors in [25] replace this pipeline paradigm with a direct strain estimation method that uses both the initial RF data and the calculated displacement field to estimate a high quality and accurate strain image in a unified framework.

The inherit advantages of direct strain estimation without computing the gradient of the displacement field has caught the attention of the researchers recently [19, 26, 27]. Most of the existing direct methods calculate the strain image by applying local/global adaptive temporal stretching of the signals in the time or frequency domain. In [19] and [26], a two-step method is proposed to use optical flow with local warping to calculate displacements and strain, simultaneously. To compensate for the signal de-correlation due to non-axial motion of tissue scatterers, in [27] the authors propose a direct average strain estimation (DASE) method using the weighted nearest neighbor method. In [28], power spectrum shift (a frequency-domain characteristic)

is estimated by cross correlation to calculate the strain image. Another frequency-domain method is discussed in [29], where the local strain is estimated by maximizing the spectral correlation between the pre- and post-compression echo signals using iterative frequency-scaling of the latter. Direct strain estimation in frequency domain can also be achieved through phase-based approaches, where the strain is modeled as a function of phase [30, 31].

All of the aforementioned papers suffer from at least one of the following shortcomings:

- Producing strain images with an acceptable SNR and CNR requires global 2D search; however, existing global search methods are not suitable for real-time applications.

- All of the existing real-time algorithms use either local search or global search on only one axial line, and unless the seed-line is placed in a carefully selected position, there is a substantial possibility that the algorithm fails.

- Most of the existing algorithms find displacement field first, and then calculate the gradient of that to compute the strain field; and this reduce the SNR and CNR of the strain image significantly.

- Without a prior information about displacement/strain field, huge jitter and false peak hopping noise will emerge, and the existing algorithms that use regularization, penalize strain (to maintain motion continuity).

To overcome these challenges, in the second part of this thesis, we introduce a 2-D strain imaging technique by minimizing an appropriate cost function which incorporates the similarity of echo amplitudes and tissue continuity. The proposed technique which we call it **SHORTCUT** (me**SH**ing **O**f g**R**adien**T** in DP for dire**C**t **U**ltrasound elas**T**ography), directly produces the strain images from RF data using a novel dynamic programming (DP) configuration. As a result, it is robust, accurate and computationally efficient. Unlike the standard DP algorithms which discretize the decision space (displacement field) and search in the space of piecewise constant functions, the proposed DP discretizes the gradient of the decision space (strain field) and searches the space of continuous piecewise-linear functions. Eliminating the displacement differentiation block and performing a global search instead of local search, which is typically done in all of the available strain estimation techniques, result in substantial improvement in SNR, CNR and accuracy of the estimations. It also substantially reduces the computational complexity. Note that the displacement images are the side product of this algorithm and they can be obtained by integrating the strain images. The accuracy and robustness of this method comes from the fact that DP is a global optimization algorithm. It is robust since it can only be locally affected by signal decorrelation caused by scatterer motion in high axial compression and non-axial motions of the probe. This is due to the fact that the proposed algorithm solves 1D DP optimization problem for each axial line independent of the results of neighboring axial lines which obstruct the propagation of a failed estimation. It is also accurate in the sense that it always finds the globally optimal estimations. However,

1D DP estimation means that the estimated strain images are not smooth laterally. Although a simple lateral averaging filter will solve the problem but, to further improve the results, a 2D DP with a special bilateral filter is used instead which uses the information of the neighboring axial lines with good performance measure to refine the estimates. Depending on the initial setting, this method can operate somewhere between a few milliseconds to a few seconds, and is thus potentially suitable for real-time elastography. It is also worth mentioning that this method is compatible with parallel computing, which can drastically decrease the computation time when multiple processors are available. The effectiveness of the proposed method is investigated through simulation data, phantom experiments, and *in vivo* patient data. The results are compared with a previous work tackling the same problem, called DPAM, which confirms the merits of the present approach.

1.1   Outline of Thesis

Following this introduction, in Chapter 2 we present an algorithm that can, under certain assumptions, generate strain images with uniform precision but varying resolution. The uniform precision property ensures that textures/variations in the strain image reflect underlying tissue properties and are not caused by errors in the displacement estimation. The algorithm has also the capability of keeping the edges between different tissue structures sharp while minimizing the noise. This is demonstrated by the phantom and in-vivo clinical data. The proposed technique is compared with

three common methods in this field, which confirm the effectiveness of the proposed algorithm. However, further clinical studies will be necessary to assess the benefits of the algorithm in practice.

In Chapter 3, we introduce a 2-D strain imaging technique based on minimizing a cost function using a novel DP technique. In the first part of this chapter, a 1D DP is proposed and in the second part the method is extended to 2D DP. In the third part of this chapter, an extensive simulation phantom study is presented followed by an experimental phantom study where the performance and behavior of the proposed method is assessed. The last part of this chapter is a clinical study on five patient data,followed by some concluding remarks. The results presented in this chapter are published in [32].

1.2   Publications

The results of this master's thesis and the author's other collaborative research during his master's work are published in or submitted to a jurnal and a number of conference proceedings [32–37] which are listed below.

- H. Khodadadi, A. G. Aghdam, and H. Rivaz, *"Ultrasound elastography: Direct strain estimation,"* IEEE Transactions on Medical Imaging, vol. In preperation, 2017.

- H. Khodadadi, A. G. Aghdam, and H. Rivaz, *"Edge-preserving ultrasonic strain*

imaging with uniform precision," in 37th Annual International Conference of the IEEE Engineering in Medicine and Biology Society (EMBC), Aug. 2015, pp. 3835-3838.

- M. Khosravi, H. Khodadadi, A. G. Aghdam, and H. Rivaz, *"Cooperative receding horizon controller for multi-target interception with obstacle avoidance,"* in proceedings of the 55th IEEE Conference on Decision and Control (CDC), Dec. 2016, pp. 93-98.

- M. Khosravi, H. Khodadadi, H. Rivaz and A. G. Aghdam, *"Cooperative Control for Multi-Target Interception with Sensing and Communication Limitations: A Game Theoretic Approach,"*, in Proceedings of the 54th IEEE Conference on Decision and Control, Dec 2015, pp. 1048-1053.

- M. Khosravi, H. Khodadadi, H. Rivaz and A. G. Aghdam, *"Maximum Reward Collection Problem: A Cooperative Receding Horizon Approach for Dynamic Clustering,"*, in Proceedings of the 2015 ACM Conference on Research in Adaptive and Convergent Systems.Oct. 2015, pp. 38-43.

- M. Khosravi, H. Khodadadi, H. Rivaz and A. G. Aghdam, *"Cooperative Receding Horizon Control of Double Integrator Vehicles for Multi-Target Interception,"* in Proceedings of the American Control Conference, July. 2015, pp. 5525-5530.

Chapter 2

Edge-Preserving Ultrasonic Strain Imaging with Uniform Precision

2.1 Introduction

Ultrasound Elastography is usually composed of two separate steps: (i) estimation of a displacement field and (ii) inferring mechanical properties from the displacement field. In this chapter we are focused on the second step in which it is common to estimate a strain image, which is the spatial derivative of the displacement field and is highly correlated with mechanical properties of tissue. A popular method for performing the spatial differentiation is piecewise-linear least square regression [38], which provides a trade-off between resolution and signal to noise ratio. Since differentiation amplifies high frequency noise, most strain estimation techniques combine differentiation with smoothing to increase the Signal-to-Noise Ratio (SNR) of the

12

strain image. An overview of common techniques for estimating high SNR strain images is provided in [39].

Previous work for estimating the strain field has two major disadvantages. First, it does not take into account the precision of the displacement field. To address this shortcoming, a technique for uniform precision strain estimation is introduced in [39], which adaptively increases the level of smoothness in regions with low precision displacement estimates. Second, smoothing blurs boundaries of edges between regions of low and high strain values. A technique for generating sharp strain images with high SNR is introduced in [7] based on Kalman filtering. The present work combines the advantages of these two techniques by introducing a uniform precision edge-preserving strain imaging technique based on bilateral filtering.

Bilateral filtering was first popularized in the computer vision community by Tomasi and Manduch [40] as an alternative to anisotropic diffusion, and has since been used in many applications in computer vision and image processing. It starts with a standard spatial Gaussian kernel, which is then modified based on image intensity values. The idea is that if a neighboring pixel has a very different intensity value compared to the center pixel, its averaging weight is reduced. Therefore, it reduces the noise while preventing over smoothing.

In this dissertation, we adaptively adjust both the *level* and *orientation* of the smoothing kernel and introduce a novel uniform precision edge-preserving strain imaging technique. Among many different variations of elastography methods, we focus on quasi-static elastography [2, 41], where tissue deformation is slow and hence

its dynamical properties can be ignored. However, the techniques that we develop here can also be applied to other variations of elastography.

This chapter is organized as follows. In the next section, we describe the our uniform precision edge-preserving filter in detail. We then provide experimental results and compare our method against both uniform precision [39] and Kalman filtering [7] strain estimation techniques using both phantom and *in-vivo* patient data. Conclusions and avenues for future work are provided in Section 2.5.

2.2   Edge-Preserving Filters

The boundary between two different tissue types is an edge in the strain image which contains useful information and must be preserved while smoothing. Failing to preserve the edges may render small targets inviable. In this section, an overview of bilateral filters for edge preserving is presented. Bilateral filtering is a technique to smooth an image while preserving edges, and can be traced back to the nonlinear Gaussian filters in the work of Aurich and Weule [42] or Tomasi and Manduchi [40] where its name was first coined. Fast versions of this filter using a piecewise-linear approximation in the intensity domain and appropriate subsampling are introduced in [43]. The underlying idea behind a bilateral filter is fairly straightforward: the intensity value at each pixel in an image is replaced by a weighted average of intensity values from nearby pixels as in nearly all smoothing filters. However, unlike other filters, the weights here depend not only on the Euclidean distance of pixels, but also

on the radiometric differences (e.g. range differences). Similar to the notion of the Euclidean distance closeness, intensity similarity the in range domain is introduced in bilateral filtering and the overall weight of a pixel in the average is computed by multiplying the spatial closeness and range similarity. This makes the filter nonlinear but preserves sharp edges because although pixels from different sides of the edges may be close in terms of Euclidean distance, their intensities are not similar. Therefore, they will have small weights in the weighted average. In other words, the smoothing will be parallel to the direction of the edge. Note that the term *range* qualifies quantities related to pixel values like intensities. The formulation of a bilateral filter is as follows [40]:

$$I^{BF}(x) = \frac{1}{W_p} \sum_{x_i \in \Omega} I(x_i) f_r(\|I(x_i) - I(x)\|) g_s(\|x_i - x\|), \qquad (2.1)$$

where W_p is the normalization factor given by:

$$W_p = \sum_{x_i \in \Omega} f_r(\|I(x_i) - I(x)\|) g_s(\|x_i - x\|). \qquad (2.2)$$

In the above equation, Ω is the window centered at x and $I(x)$, $I^{BF}(x)$ are the original and filtered images, respectively. Moreover, functions $f_r(\cdot)$ and $g_s(\cdot)$ are the range and spatial kernel for smoothing difference in intensities and coordinates, respectively. Gaussian functions are good candidates for the spatial and range kernel as they give a low weight to pixels that are either spatially far or have dissimilarity in photometric

range. Therefore, those two functions are chosen as follows:

$$f_r(x) = G_{\sigma_r}(x) = \frac{1}{2\pi\sigma_r^2} e^{-\frac{x^2}{2\sigma_r^2}}, \tag{2.3a}$$

$$g_s(x) = G_{\sigma_s}(x) = \frac{1}{2\pi\sigma_s^2} e^{-\frac{x^2}{2\sigma_s^2}}. \tag{2.3b}$$

The bilateral filter with Gaussian functions has two parameters: σ_r and σ_s. The spatial spread σ_s is chosen based on the desired amount of smoothness or low-pass filtering. A large σ_s would include the intensities of pixels from more distant image locations in the domain. Similarly, the photometric spread σ_r in the image range determines how close in range the pixels should be in order to be considered as similar pixels. Figure 2.1(a) shows an example of a simple gray-scale image with an edge in the middle which is perturbed by Gaussian noise. Figure 2.1(b) depicts the result of applying a bilateral filter with $\sigma_r = 0.1$ and $\sigma_r = 10$ to this image and Figure 2.1(c) shows the kernel of the bilateral filter at a point located on the edge in which it is clear that only the weight of the pixels that are located at one side of the edge are non-zero; therefore, the edge will be untouched.

2.3   Uniform Precision Edge-Preserving Filter

In this section, first a method for calculating the precision is reviewed, and then the main contribution of this chapter, which is a proper integration of both edge-preserving and uniform precision in one filter, is presented.
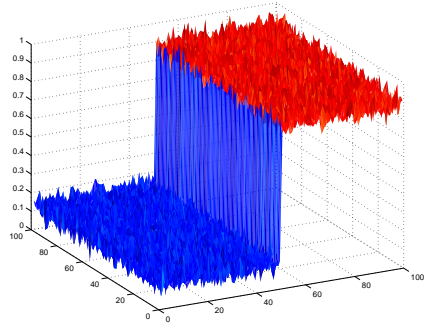
(a)
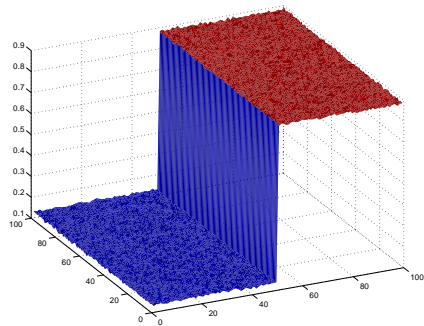
(b)
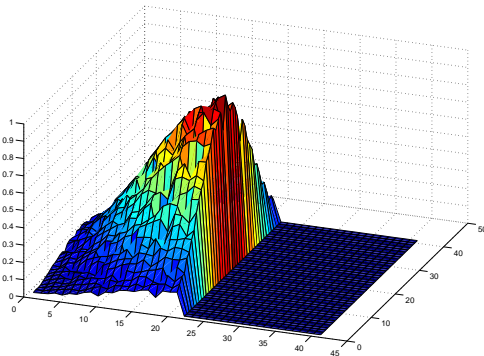
(c)

Figure 2.1: (a) An example of a gray-scale image; (b) smoothed image filtered by a bilateral filter, and (c) Gaussian kernel at the edge of the image $I(50, 50)$.

It was shown in [44] that the precision p of the displacement data can be estimated, under some simplifying assumptions, from complex cross-correlation ρ of matched displacement windows of pre- and post-deformation data. The precision $p(x, y)$ and cross-correlation $\rho(x, y)$ can be computed as follows [44]:

$$\rho(\Omega_n, \hat{d}_n) = \frac{\sum_{\{x,y\} \in \Omega_n} I_1(x, y) I_2(x + \hat{d}_n^x, y + \hat{d}_n^y)}{\frac{1}{2} \sum_{\{x,y\} \in \Omega_n} |I_1(x, y)|^2 + |I_2(x + \hat{d}_n^x, y + \hat{d}_n^y)|^2}, \tag{2.4}$$

$$p(x, y) = \frac{\rho(\Omega_n, \hat{d}_n)}{1 - \rho(\Omega_n, \hat{d}_n)}, \tag{2.5}$$

where Ω_n is the displacement window, I_1, I_2 are the pre- and post-deformation images, and $\hat{d}_n^x$, $\hat{d}_n^y$ are the estimated axial and lateral displacements, respectively. In this work, the assumption of negligible lateral displacement in [44] and [39] is relaxed since both axial and lateral displacements are calculated.

Knowing the precision, the goal is to adapt the smoothing to the precision of the image while keeping the edges untouched. The adaptation mechanism should blur the regions with low precisions while preserving the regions of high precision. The range kernel is in charge of the edge-preserving function of the filter and should remain untouched. Since the level of smoothing is related to the spatial kernel of the bilateral filter, adapting the parameter σ_s to the precision of the image seems to be a logical approach. When the precision is high, the parameter σ_s should be low, and vice-versa. The only difficulty that remains is defining the mathematical

18

relationship between σ_s and p. Suppose that a Gaussian blur is used to smooth an image. The cut-off frequency of this linear low-pass filter in each direction is $f_c \propto \frac{1}{\sigma_s}$, and consequently the resolution in each direction will be $R \propto \sigma_s$, where σ_s is the Gaussian spatial spread. Now, suppose the raw strain data contains independent measurements from the same relatively homogeneous strain distribution. The filtered strain precision in such cases will scale with the size of the Gaussian kernel width. Note that the 2D kernel will have a size proportional to the square of the 1D kernel size [39]. Bearing in mind that the kernel size is proportional to the spatial spread, if the precision of the original image was p_0, the precision of the smoothed image would be:

$$p(x,y) \propto p_0(x,y)\sigma_s^2(x,y). \tag{2.6}$$

This leads to:

$$\sigma_s(x,y) = \frac{k}{\sqrt{p_0(x,y)}}. \tag{2.7}$$

Substituting (2.7) in (2.6) will cancel out the initial precision $p_0(x,y)$ from Eq. (2.6) and therefore a uniform precision image can be produced. The precision scaling factor k can tune the level of overall precision after smoothing.

The above reasoning for Gaussian blur can be extended to the bilateral filter because the range kernel does not change the spatial kernel size. Note that the computation time of this approach is less than or equal to that of a bilateral filter because the size of the kernel is reduced when the image has certain degree of precision.

19

Figure 2.2: The result of different methods applied to the phantom data: (a) The axial displacement; (b) the raw strain data calculated by simple discrete differentiation of the axial displacement; (c) the precision image; (d) the result of the least-squares method applied to the axial displacement; (e) the result of the least-squares method with Kalman filter applied to the axial displacement, and (f) the result of the proposed uniform precision edge-preserving filter applied to the raw axial strain image.

It should be noted that a precision value of zero results in $\sigma_s = \infty$ in eq. (2.7). In practice, σ_s cannot be infinity; thus, a maximum spatial spread is defined, denoted by σ_{max}, and any value higher than that is substituted by σ_{max}.

2.4 Experimental Results

In this section, phantom results and patient trail are presented. The RF data is acquired from an Antares Siemens system (Issaquah, WA) at the center frequency of 6.67 MHz with a VF10-5 linear array at a sampling rate of 40 MHz. To evaluate the proposed filter, first the 2D AM method introduced by Rivaz et al. [7] is used to produce axial and lateral displacement images from the RF data, and then the proposed method is applied to the displacement images to calculate the precision and the strain. To compare the results, two other methods are also applied to the data which are as follows:

1. *Least-squares method*: This isthe most common approach that is used for generating the strain image from the displacement image. Roughly speaking, the least-squares method computes the strain in each pixel by calculating the slope of a line fitted to the displacement data of a window in the axial direction. To make the strain more accurate, the line window could be a plane in 2D, where the strain is calculated for the center of the plane.

2. *Least squares with Kalman filter*: This approach, originally proposed by Rivaz et al. [7], further smoothes the resulting strain of the least squares in the lateral

direction. The Kalman filter is used as it has the ability to keep the edges while smoothing the rest of the image.

A Gaussian blur filter is used to pre-process the strain image, and due to the fact that the strain image is produced by calculating the displacement in the axial line, the resulting strain image needs more smoothing in the lateral direction so an asymmetric kernel is used for the filter.

In the experiments, the parameters of 2D AM are set to $\alpha = 5$, $\beta_a = 10$, $\beta_l = 0.005$, and $T = 0.2$ (eqs. (12) and (20) in [7]), and the tunable parameters of the DP are chosen as $\alpha_\alpha = \alpha_l = 0.15$ (eq. (1) in [7]). In the precision calculation the window size is $\Omega = 40$, while the spatial and range spreads in the bilateral filter can adapt to the image properties ($\sigma_s = \frac{Width(I)}{10}$, $\sigma_r = \frac{I_{max}-I_{min}}{16}$). Finally, in the proposed filter, the maximum spatial spread is $\sigma_{max} = 30$, the range spread adapts to the image ($\sigma_r = \frac{I_{max}-I_{min}}{16}$) and the scaling factor of precision is $k = 3$.

2.4.1 Phantom Data

Figure 2.2 shows the phantom results obtained by different methods. It can be observed from this figure that the least-squares method produces a somehow smooth strain data with very blurry edges. Furthermore, the least squares with Kalman filter output is more or less the same as that of least-squares operation, but is more smooth in the lateral direction. It is worth noting that the Kalman filter tends to keep the edges untouched when smoothing in the lateral direction. Figure 2.2(f) depicts the
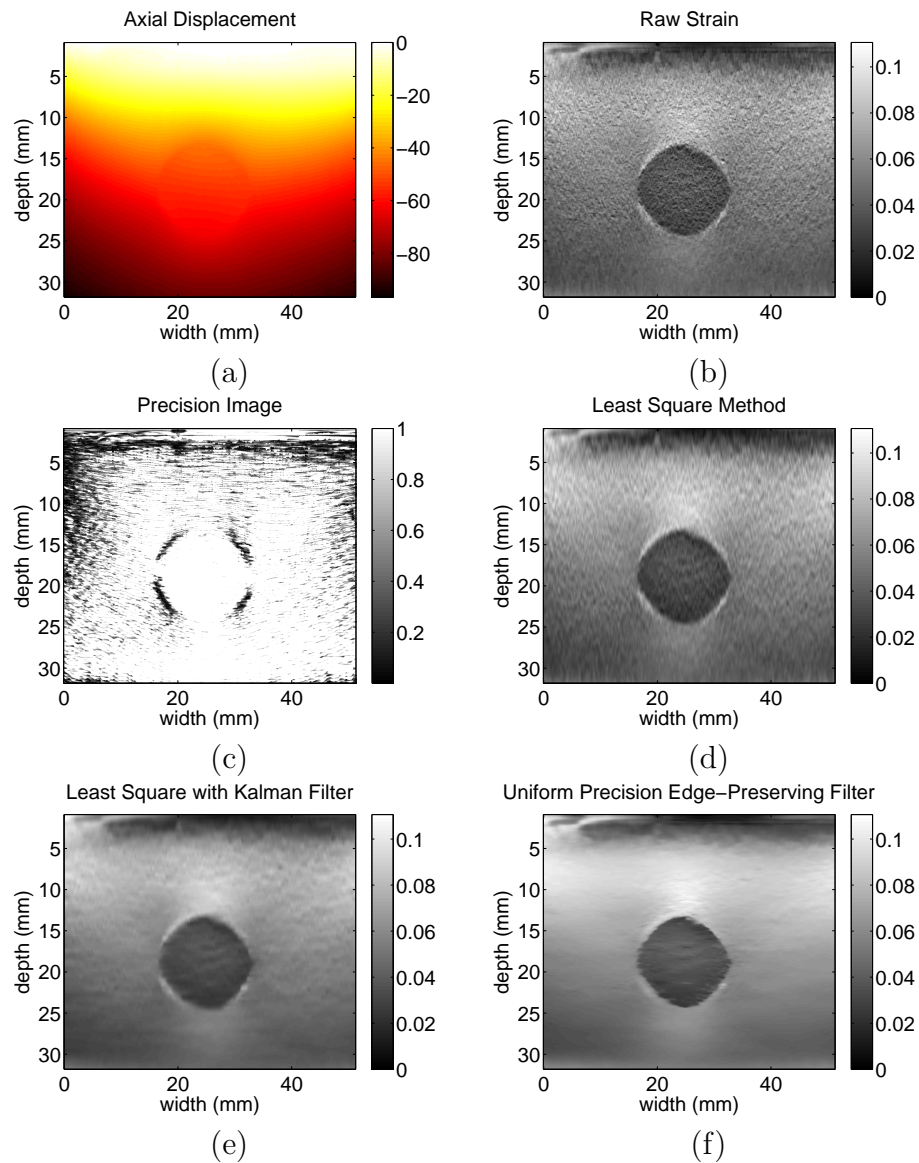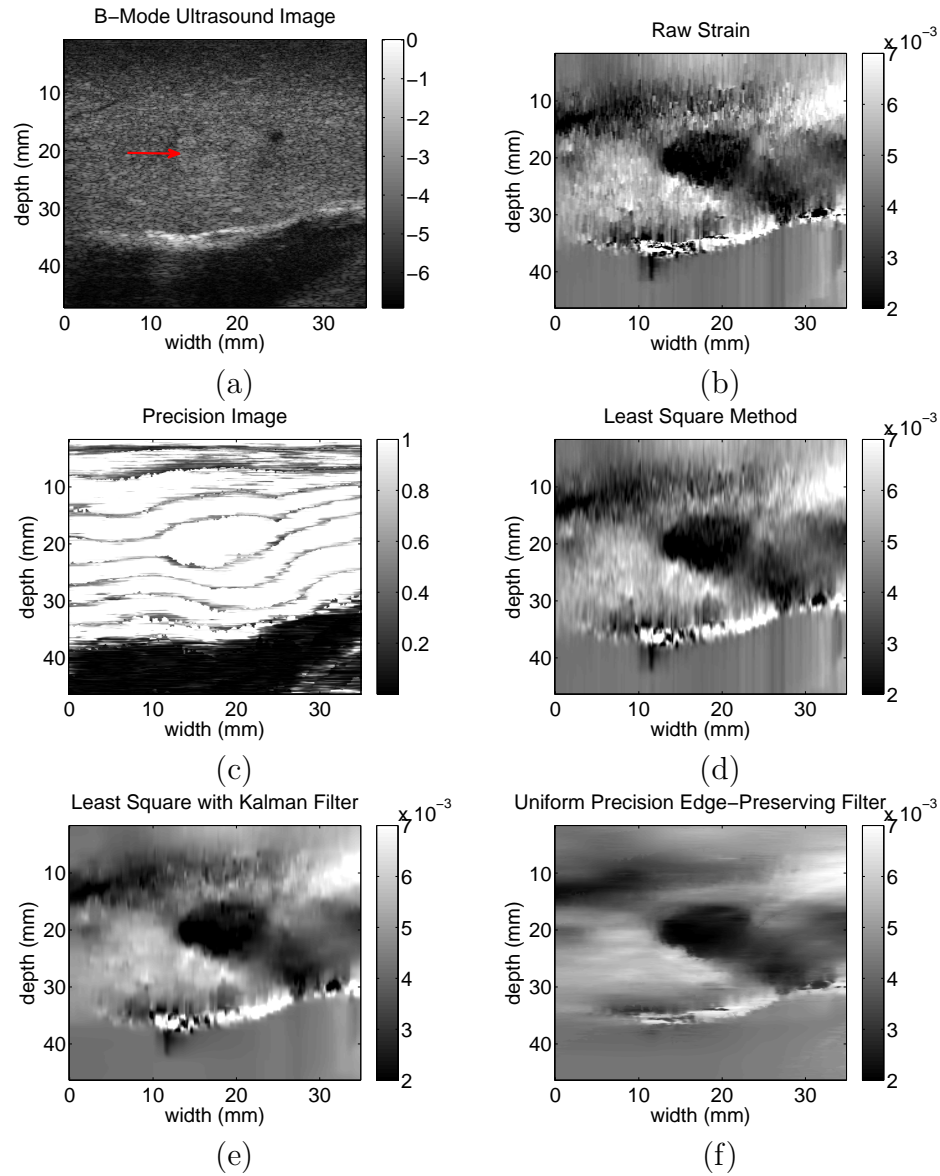
Figure 2.3: The result of different methods applied to the patient data. (a) The Axial displacement generated; (b) the raw strain data calculated by simple discrete differentiation of the axial displacement; (c) the precision image; (d) the result of the least-squares method applied to the axial displacement; (e) the result of the least-squares method with Kalman filter applied to the axial displacement, and (f) the result of the proposed uniform precision edge-preserving filter.

result of the proposed uniform precision edge-preserving filter applied to the raw axial strain image. The uniform precision property of the filter is not distinguishable here because the precision of the phantom result is already somehow uniform (Figure 2.2(c)).

2.4.2 In-vivo Data

The data is acquired from patients undergoing open surgical radiofrequency (RF) thermal ablation for primary or secondary liver cancer. We are thankful to Drs. Boctor and Choti from Johns Hopkins Hospital for sharing the data with us. Figure 2.3 shows the ultrasound and strain images of a patient before ablation. A hard tumor, marked with an arrow, is hardly visible in the ultrasound image. The result of applying different methods to this data clearly shows the merits of the proposed uniform precision edge-preserving filter. Figure 2.3(f) offers a more informative and less decisive image for the diagnostic applications, because it smoothes the unreliable noisy regions while keeping the information of the precise regions and the edges untouched.

2.5 Conclusions

In this chapter, we present an algorithm that can, under certain assumptions, generate strain images with uniform precision but varying resolution. The uniform precision property ensures that textures/variations in the strain image reflect the underlying tissue properties and are not caused by errors in the displacement estimation. The

algorithm can also keep the edges between different tissue structures sharp while minimizing the noise. This is demonstrated by the phantom and in-vivo clinical data. The results are compared with three common methods in this field of research, confirming the effectiveness of the proposed algorithm. However, further clinical studies will be necessary to assess the benefits of the algorithm.

Chapter 3

Ultrasound Elastography: Direct Strain Estimation

3.1 Introduction

Assume two consecutive ultrasound Radio-Frequency(RF) echo field $I_1(i,j) : i \in \mathbb{N}^{\leq m} \times j \in \mathbb{N}^{\leq n} \to \mathbb{R}$ and $I_2(i,j) : i \in \mathbb{N}^{\leq m} \times j \in \mathbb{N}^{\leq n} \to \mathbb{R}$, which are taken before and after the tissue undergoes a deformation. Define $A^{m \times n} \in \mathbb{R}$ and $L^{m \times n} \in \mathbb{R}$ as the axial and lateral displacement matrices (the out-of-plane motion is not considered here) where each of their elements $a_{i,j}$ and $l_{i,j}$ satisfy $\|a_{i,j}\| \leq a_{\max}$ and $\|l_{i,j}\| \leq l_{\max}$, and $a_{\max}$ and $l_{\max}$ are the maximum possible axial and lateral displacement estimates, respectively.

The ultrasound elastography problem deals with finding these two matrices (A and L) such that $I_1(i,j) = I_2(i + a_{i,j}, j + l_{i,j})$. Note that calculating $I_2(i + a_{i,j}, j + l_{i,j})$

may need a sub-pixel interpolation of I_2. we write this as an optimization problem using a simple cost function as follows:

$$\min_{A,L} P = \min_{A,L}[\Phi(I_1, I_2, A, L) + \alpha\Psi(A, L)] \tag{3.1}$$

where the first term $\Phi(I_1, I_2, A, L)$ is a penalty function for speckle decorrelation, assuming echo signals can be fully restored, and the second term $\Psi(A, L)$ is a penalty function for losing motion continuity and α is the weight of regularization. This optimization problem was solved by a dynamic programming technique named the Viterbi algorithm [45]. Dynamic programming (also known as dynamic optimization) is a method based on Bellman's principle of optimality [46] for solving a complex problem by breaking it down into a collection of simpler subproblems such that each subproblem corresponds to a discrete decision, solving each of those subproblems just once, storing their solutions (memorization) and reusing them next time the same subproblem occurs. The decisions should follow each other sequentially and the cost corresponding to each decision should only depend on the previous and not the future decisions (causality). This approach can usually save computation time at the expense of a modest expenditure in storage space. As shown in Figure 3.1, costs will be calculated going forward in two adjacent data points using eq. (3.1). To save computing time, these values will be stored in a 3D array $C_i^j(k)$ and the Viterbi algorithm can efficiently trace back the global optimum solution from $i = n$ to $i = 1$(See the thick line path in Figure 3.1). This algorithm was selected because

of its efficiency and simplicity. It is important to note that this optimization process will only be used to determine the displacement vector in integer precision due to the nature of the Viterbi algorithm. In [21], this algorithm is used to find the displacement matrices A and L in integer precision. The formulation of this algorithm is as follows. Assuming that ultrasound images consist of n A-lines, we define data and smoothness terms as follows

$$\Delta(i,j,a_{i,j},l_{i,j}) = |I_1(i,j) - I_2((i + a_{i,j}, j + l_{i,j})|\,,\tag{3.2}$$

$$S(a_{i,j},l_{i,j},a_{i-1,j},l_{i-1,j}) = (a_{i,j} - a_{i-1,j})^2 + (l_{i,j} - l_{i-1,j})^2.\tag{3.3}$$

The cost function at the ith sample of the jth A-line is

$$C_i^j(a_{i,j},l_{i,j}) = \Delta(i,j,a_{i,j},l_{i,j}) + \min_{\delta_a,\delta_l}\left\{ \frac{C_{i-1,j}(\delta_a,\delta_l) + C_{i,j-1}(\delta_a,\delta_l)}{2} + \alpha S(a_{i,j},l_{i,j},\delta_a,\delta_l)\right\}.$$
$$\tag{3.4}$$

In this chapter, using a novel DP configuration, we introduce a fast, robust and accurate direct 2-D strain imaging technique called SHORTCUT (me**SH**ing **O**f g**R**adien**T** in DP for dire**C**t **U**ltrasound elas**T**ography) based on minimizing a cost function. The cost function incorporates similarity of echo amplitudes and tissue continuity. Unlike the standard DP algorithm which discretizes the decision space (displacement field) and search in the space of piecewise constant displacement functions, the proposed DP discretizes the gradient of the decision space (strain field) and searches the space of continuous piecewise linear displacement functions. Eliminating the displacement
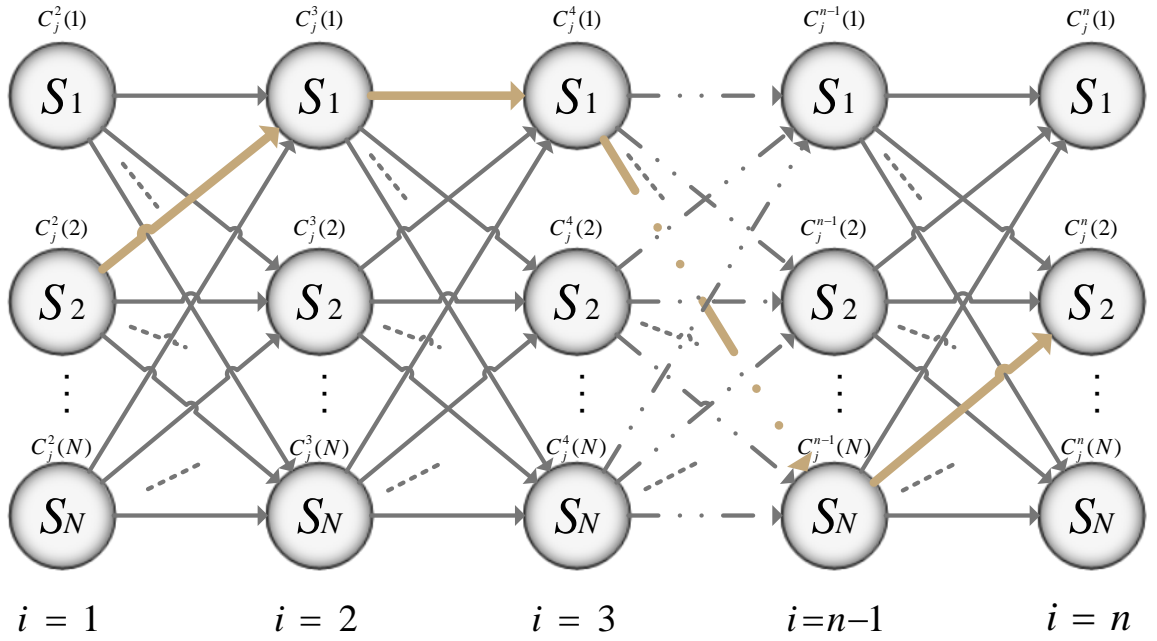
Figure 3.1: An illustration of the Viterbi algorithm. Here, i represents different steps where the optimum state should be simultaneously estimated and S_N represents N possible selections of states for each step. The cost in each state (circles) is determined by eq. (3.1) and it is the minimum cost of reaching that state from any previous step state. To save computing time, these values will be stored in a 3D array $C_i^j(k)$ and the Viterbi algorithm can efficiently trace back the global optimum solution from $i = n$ to $i = 1$(See the thick line path).

differentiation block and performing a global search instead of local search which exist in all of the available strain estimation techniques result in substantial improvement in SNR, CNR and accuracy of the estimations. Note that the displacement images are the side product of this algorithm and they can be obtained by integrating the strain images. The robustness of this method comes from the fact that DP is global optimization algorithm. Therefore, not only its accurate in the sense that it always finds the globally optimal estimations but also it can only be locally affected by signal decorrelation (caused by scatterer motion in high axial compression and non-axial motions of the probe). This is due to the fact that the proposed algorithm solves 1D DP optimization problem for each axial line independent of the results of neighboring axial lines which obstructs the propagation of a failed estimation. However, 1D DP estimation means that the estimated strain images are not smooth laterally. Although a simple lateral averaging filter will solve the problem to some extent, to further improve the results, a 2D DP with a special bilateral filter is used instead which use the information of the neighboring axial lines with good performance measure to refine the estimates. Given different initial settings this method can operates somewhere between a few milliseconds to a few seconds and is thus also potentially suitable for real time elastography.

This chapter consist of three sections. the first section deals with the proposed 1D SHORTCUT. The second section improve the estimation by introducing a 2D SHORTCUT. The effectiveness of the proposed method is investigated in section three

30

through simulation data, phantom experiments, and *in vivo* patient data whereby the results are compared with a similar previous work called DPAM [7].

3.2   1D SHORTCUT

Consider two echo signals corresponding to two A-lines acquired before and after compression. A 1D DP is formulated in which the axial strain field and lateral displacement is discretized. Assume the possible axial strain values lies in the interval $[a^{\min}, a^{\max}]$. Let also the set $\mathcal{S} = \{a_k : a^{\min} < a_k < a^{\max}\}_{k=1}^N$ which partition the strain space into $N+1$ intervals. Similarly, assume the set $\mathcal{L} = \{l_k : l^{\min} < l_k < l^{\max}\}_{k=1}^M$ partition the lateral displacement field into $M+1$ intervals where $l^{\min}$ and $l^{\max}$ are the minimum and maximum possible lateral displacement values. Displacement field is needed to calculate the similarity measure in the cost function and the main idea of the new DP method is to discretizes the gradient domain (strain) instead of displacement. Therefore, the proposed method needs an initial condition on the first step of DP. Fortunately, here we know that the first step in axial line always have zero displacement, however in the lateral search this is not the case i.e. we do not know the lateral initial condition a-priori. Therefore the possible states in 3.1 are combination of discretized axial strain and lateral displacement i.e. $\mathcal{S} \times \mathcal{L}$. Lateral displacement always has much lower SNR and CNR than axial since the displacement in lateral direction is very small and also because the resolution of the ultrasound is low in the lateral direction. Therefore it is only computed to improve

the axial displacement which means that subsample estimation in the lateral direction is not necessary. Similar to eqs. (3.4) and (3.1), the new DP cost function consists of speckle decorrelation (the brightness difference between the two signals) term and regularization term and both are formulated as sum of absolute differences (SAD) which is computationally inexpensive to compute and has been shown to have good robustness against outliers [47]. The proposed 1D DP cost function is proposed as follows

$$C_j^i(a_{ij}, l_{ij}) = \frac{|I_1(i,j) - I_2(i + \lfloor D(a_{ij}) \rfloor, j + l_{ij}) - \acute{I}_2(i + \lfloor D(a_{ij}) \rfloor, j + l_{ij})\{D(a_{ij})\}|}{I_1^{\text{env}}(i,j)}$$

$$+ \min_{s_a, d_l} \left[C_j^{i-1}(s_a, d_l) + R_j(a_{ij}, l_{ij}, s_a, d_l) \right],$$

$$\tag{3.5}$$

$$R_j(a_{ij}, l_{ij}, s_a, d_l) = \alpha_a |a_{ij} - s_a| + \alpha_l |l_{ij} - d_a|. \tag{3.6}$$

where $D(a_{ij}) = \sum_{k=0}^{i} a(k,j)$ is the axial displacement and $a_{0j} = 0$ and I_1^{env} is the envelope of I_1 used for normalization of the error. Note that $\lfloor D(a_{ij}) \rfloor$ and $\{D(a_{ij})\} = D(a_{ij}) - \lfloor D(a_{ij}) \rfloor$ represent the floor and fraction part of $D(a_{ij})$. Note also that minimization of the above cost function will provide both axial strain and lateral displacement on the j Axial line and a_{ij} and l_{ij} can take values from set $\mathcal{S}$ and $\mathcal{L}$, respectively.

3.3   2D SHORTCUT

The 1D SHORTCUT presented in the previous section will simultaneously estimate both axial strains and lateral displacements in any axial RF-line, however, this leads to two shortcomings. First, estimating strains and displacements on individual RF-lines, 1D SHORTCUT only utilizes a small fraction of the information available from the entire image. Second, regularizing the axial strain and lateral displacement only on the axial direction results in discontinuous estimation between adjacent RF-lines which produce visible artifacts in the form of vertical streaks in the resulting images. Note that when substantial signal decorrelation exists in the specific axial line not only the vertical artifact can be more prominent but also insufficient information may cause the 1d SHORTCUT to fail on that specific axial line. The DP cost function eq. (3.5) of the previous subsection is modified here to allow for 2-D estimation and smoothness regularization:

$$C_j^i(a_{ij}, l_{ij}) = \frac{|I_1(i,j) - I_2(i + \lfloor D(a_{ij}) \rfloor, j + l_{ij}) - \acute{I}_2(i + \lfloor D(a_{ij}) \rfloor, j + l_{ij})\{D(a_{ij})\}|}{I_1^{\mathrm{env}}(i,j)}$$

$$+ \min_{s_a, d_l} \left[C_j^{i-1}(s_a, d_l) + R_j(a_{ij}, l_{ij}, s_a, d_l) \right],$$

$$(3.7)$$

$$R_j(a_{ij}, l_{ij}, s_a, d_l) = \sum_{k \in \Omega} [\alpha_a \omega_k |a_{i(j+k)} - s_a| + \alpha_l \omega_k |l_{i(j+k)} - d_a|], \qquad (3.8)$$

where Ω is a 1D lateral window centered at axial line j and ω_k are lateral regularization weights computed by the following 1D bilateral filter [40]:

$$\omega_k = \frac{f_r(\|R(j+k) - R(j)\|)g_s(\|k\|)}{W_p}, \tag{3.9}$$

where the W_p is the normalization factor

$$W_p = \sum_{x_i \in \Omega} f_r(\|R(j+k) - R(j)\|)g_s(\|k\|) \tag{3.10}$$

and

$$\mathcal{R}(j) = \sum_{i=1}^{n} \frac{|I_1(i,j) - I_2(i + \lfloor D(a_{ij}^*) \rfloor, j + l_{ij}^*) - \acute{I}_2(i + \lfloor D(a_{ij}^*) \rfloor, j + l_{ij}^*)\{D(a_{ij}^*)\}|}{I_1^{\text{env}}(i,j)}, \tag{3.11}$$

is the residual of the jth axial line computed from the optimal values found by the 1D SHORTCUT. Functions f_r and g_s are the error and spatial kernel, respectively. Gaussian functions are good candidate for both the spatial and error kernels as they give a low weight to pixels that are either spatially far or have high output residual. Note that relatively high residual in any pixel means that due to higher signal decorrelation the 1D SHORTCUT has not been able to find a good estimates compare to its neighbors:

$$f_r(x) = G_{\sigma_r}(x) = \frac{1}{2\pi\sigma_r^2}e^{-\frac{x^2}{2\sigma_r^2}}, \tag{3.12}$$

$$g_s(x) = G_{\sigma_s}(x) = \frac{1}{2\pi\sigma_s^2} e^{-\frac{x^2}{2\sigma_s^2}}. \tag{3.13}$$

The bilateral filter with Gaussian functions has two parameters: σ_r and σ_s. The spatial spread σ_s is chosen based on the desired amount of smoothness or low-pass filtering. A large σ_s includes the intensities of pixels from more distant locations in the domain. Similarly, the residual spread σ_r determines how close the residual of any adjacent axial line should be to the minimum residual found in that window to contribute meaningfully in the lateral regularization. Its worth mentioning that σ_r is not fixed and will be updated for each window.

3.4   Simulation Results

Simulation phantoms can help assessing the performance of the proposed approach since they provide a ground truth strain image. Two simulation phantom are needed which correspond to the pre and post-compression ultrasound images. The first ultrasound RF-data is created using Field II [48] software by distributing numerous scatterers in a volume and passing them through a filter with the point spread function of the ultrasound probe as its kernel. The parameters of the ultrasound probe are set to mimic commercial probes. The probe frequency is 7.27 MHz, the sampling rate is $40MHz$ and the fractional bandwidth is 60%. ABAQUS (Providence, RI) software is then utilized to mesh and compress the resulting ultrasound image using

finite element simulation. The outcome of the finite element simulation is the 3D displacement of the mesh nodes and in order to find the displacement of each scatterer, displacement of its neighboring nodes are interpolated. Finally, the second ultrasound image is generated by moving the scatterers according to their corresponding displacements.

In this section. the displacement and strain fields are calculated using the proposed method and are compared with the ground truth and DPAM method [7]. The unitless metric signal-to-noise ratio (SNR) and contrast to noise ratio (CNR) are also calculated to better assess the performance of the methods according to

$$CNR = \frac{C}{N} = \sqrt{\frac{2(\bar{s}_b - \bar{s}_t)^2}{\sigma_b^2 + \sigma_t^2}}, \tag{3.14}$$

$$SNR = \frac{\bar{s}}{\sigma}, \tag{3.15}$$

where σ_t^2 and σ_b^2 are the spatial strain variance of the target and background, $\bar{s}_t$ and $\bar{s}_b$ are the spatial strain average of the target and background, and $\bar{s}$ and σ are the spatial average and variance of a window in the strain image, respectively.

Figure 3.2 depicts the B-mode RF images of the simulation phantom before and after compression. The results of both DPAM and the proposed 1D SHORTCUT method are represented in Figure 3.3 in which the first row compares the axial images produced by the two approached with the ground truth. As one can see not only the proposed method outperforms the DPAM approach in terms of the SNR and CNR, but also it preserved the fine boundaries of the simulated blood vessel very well. It's
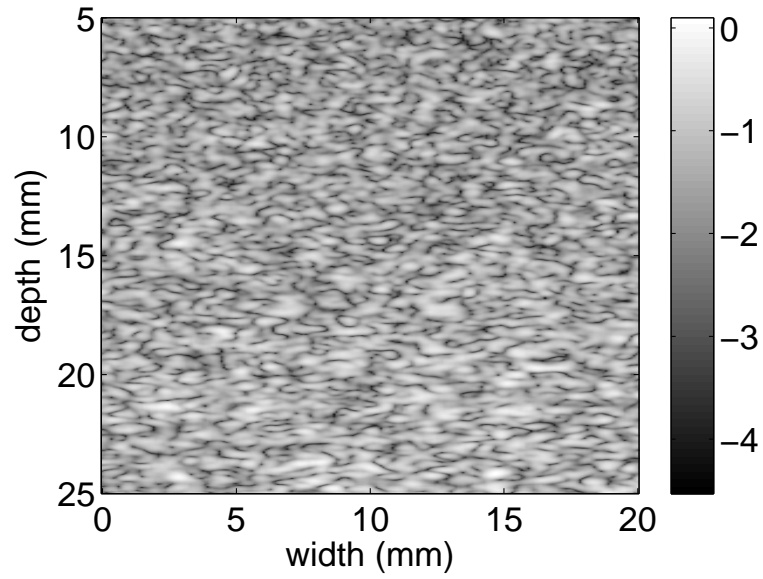
(a)
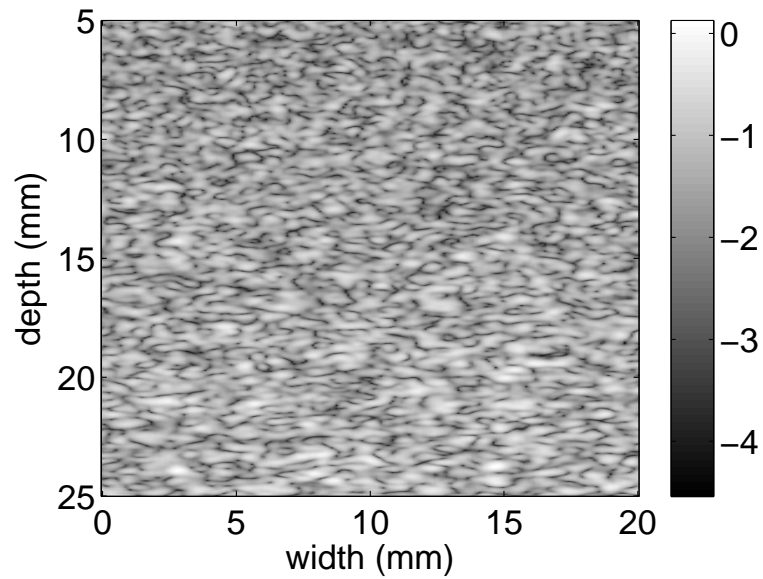
(b)

Figure 3.2: Simulation Phantom B-Mode (a) Pre-Compression (b) Post-Compression
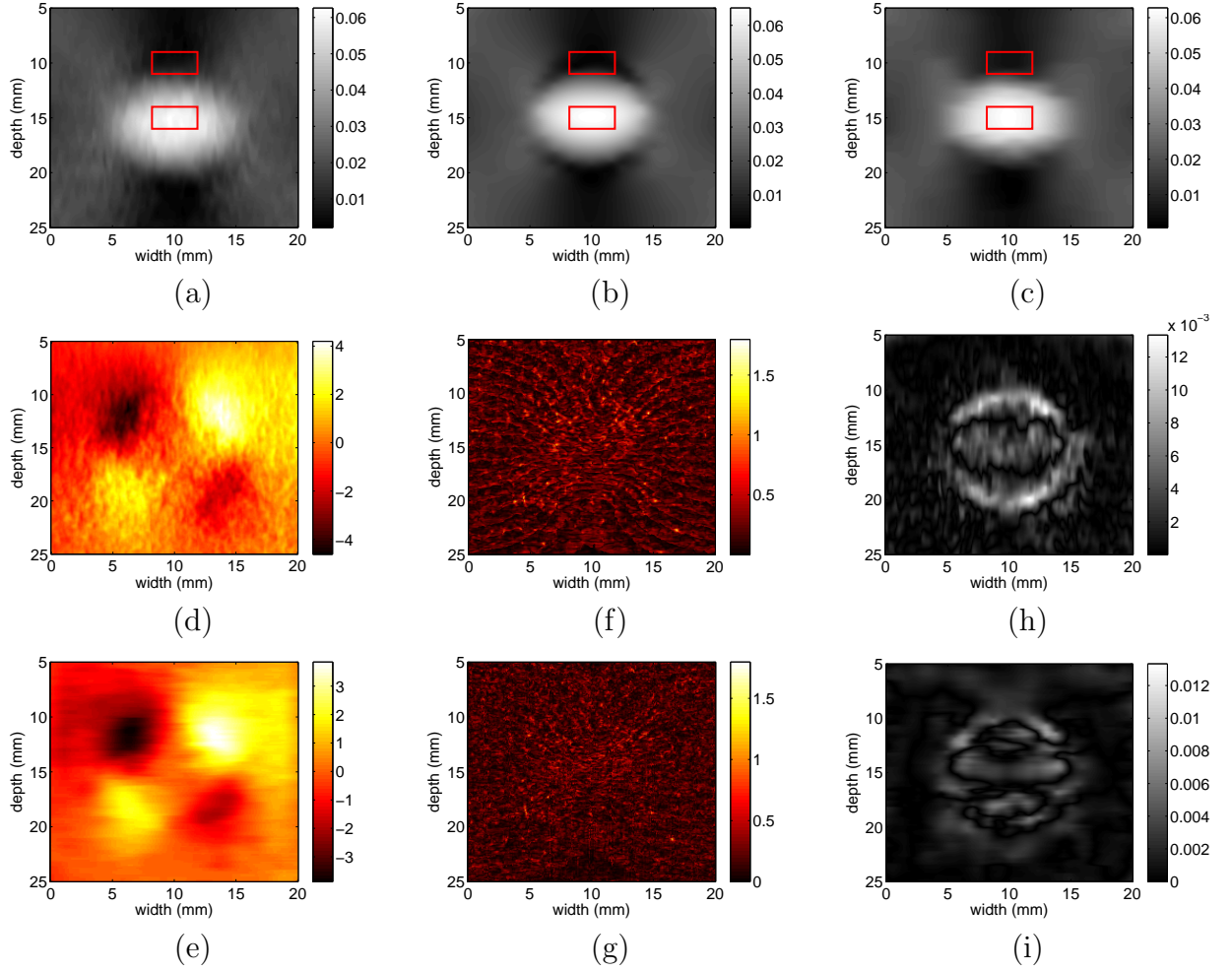
Figure 3.3: The result of different methods applied to the simulation phantom data: (a) Axial strain of the DPAM approach (b) Ground Truth stain image (c) Axial strain of the SHORTCUT approach (d) Lateral displacement of the DPAM approach(e) Lateral displacement of SHORTCUT approach (f) Logarithm of absolute residual in DPAM (g) Logarithm of absolute residual in SHORTCUT (h) Absolute Error of DPAM strain image w.r.t. the Ground Truth (i) Absolute Error of SHORTCUT strain image w.r.t. the Ground Truth.

worth mentioning that the result of 1D SHORTCUT method is smoothed laterally by a simple averaging filter of kernel size 7 and $\sigma = 3$. Other parameters of eq. (3.5) are set to $\alpha_a = 0.5, \alpha_l = 1.4$.

The SHORTCUT algorithm globally minimize a cost function, eq. (3.5), which is composed of normalized residuals, eq. (3.11) (i.e., the intensity similarity measure), and the regularization terms eq. (3.6). In other words the regularization terms constrain the space of admissible strain images and the resulting optimized strain image will not necessarily minimize the residuals. Figure 3.3(f)-(g) compares the normalized residuals of the two method. Note that in order to better show the detail of the residual pattern, the intensity of these images are scaled logarithmically. The layered patterns in 3.3(f) reveals in the DPAM approach was not able to fully capture the RF data information. The residual image of 1D SHORTCUT is depicted in 3.3(g) and it almost resemble a white noise which means that it had been able to capture all the information of the RF data. Lastly, 3.3(h)-(i) show the absolute error between the ground truth and DPAM, SHORTCUT method, respectively. The DPAM approach have been vulnerable around the boundaries of the simulated blood vessel. To better visualize the accuracy of the estimation a 3d presentation of the ground truth strain and the results of both DPAM and 1D SHORTCUT is showed in Figure 3.4

Table 3.1 shows substantial improvement in the SNR (15.51%) and CNR (18.71%) of the strain maps produced by 1D SHORTCUT compared to DPAM. Note that the SNR and CNR of the ground truth strain image with the same target and background boxes are 37.08% and 27.08%, respectively. In order to quantify the strain estimation
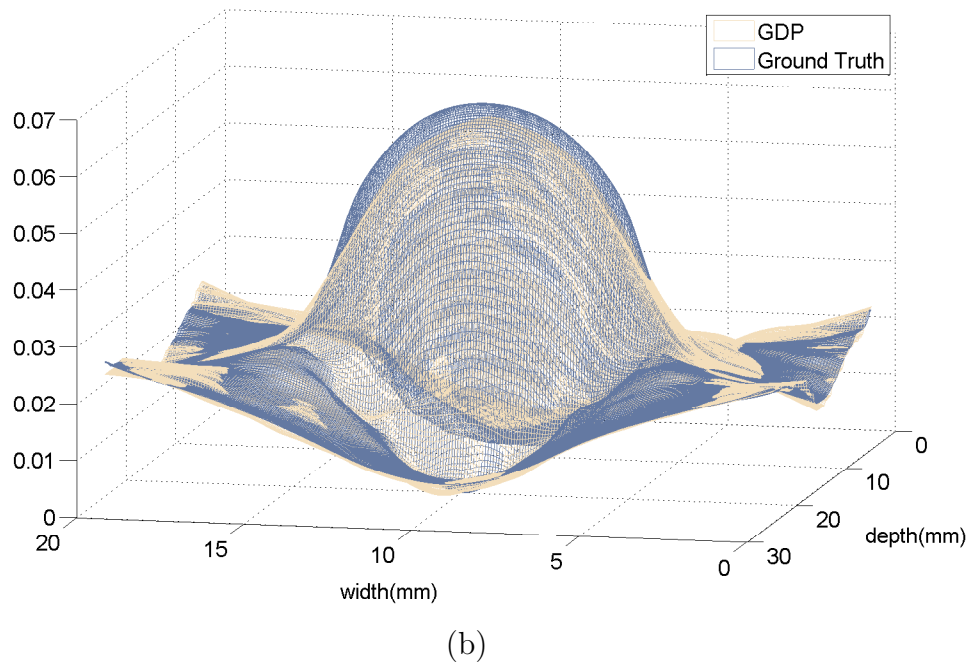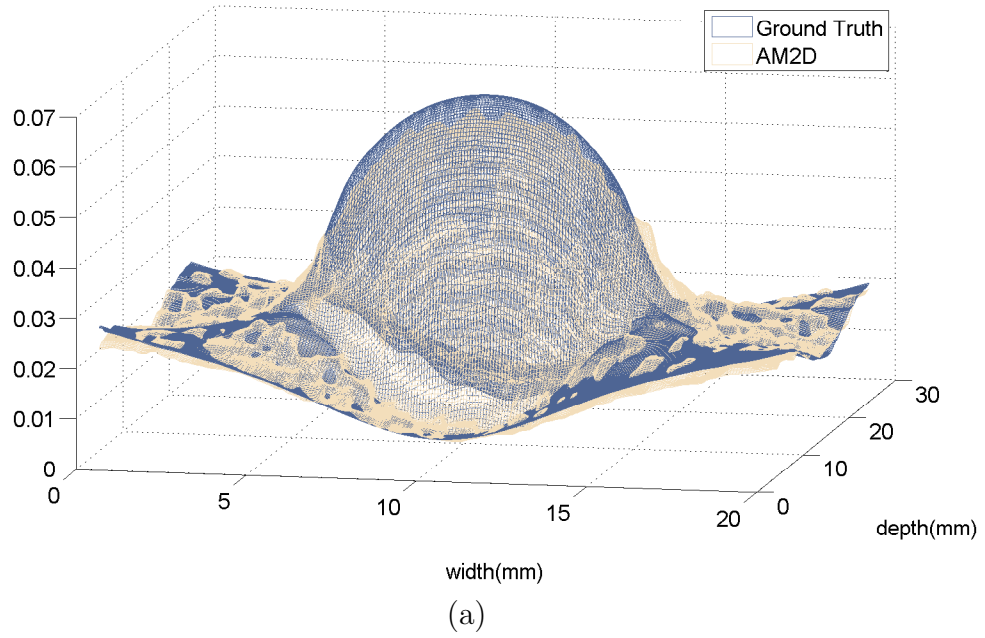
Figure 3.4: Simulation Phantom strain profile (a) DPAM (b) SHORTCUT

Table 3.1: The Simulation phantom results of DPAM and 1D SHORTCUT approach are compared in terms of SNR, CNR, residual mean, residual median. The Normalized Mean Absolute Error(NMAE) of the strain images w.r.t. the ground truth are also reported in percentage. Target and background windows used for CNR calculation are shown in Figure 3.3.

Method	SNR	CNR	Residual Mean	Residual Median	NMAE
DPAM	42.47	23.35	0.2354	0.1693	7.78%
SHORTCUT	49.055	27.72	0.195	0.149	6.10%
Improvement %	15.51%	18.71%	17.16%	12%	21.6%
Ground Truth	37.38	27.08	-	-	-

accuracy, Normalized Mean Absolute Error (NMAE) is defined as follow:

$$\text{NMAE} = 100\%.\frac{\Sigma_{i=1}^{m}\Sigma_{j=1}^{n}|I_{\text{estimated}}^{i,j} - I_{GT}^{i,j}|}{\Sigma_{i=1}^{m}\Sigma_{j=1}^{n}I_{GT_{i,j}}}, \qquad (3.16)$$

where $I_{GT}^{i,j}$ and $I_{\text{estimated}}^{i,j}$ are the intensity of the i,j pixel in the ground truth and estimated image, respectively. This measure by definition represents the absolute accuracy error one should expect to have in percentage. The last column in Table 3.1 shows a 21.6 percent improvement in the accuracy of the proposed method compared to the DPAM.

3.4.1 The effect of changing the regularization coefficient

In order to assess the robustness of the proposed algorithm, the effect of changing the regularization parameter α_a in eq. (3.6) on the performance of the proposed 1D SHORTCUT is considered. The regularization coefficient together with N which determine the number of discretizes strain values sampled uniformly from the interval $[a^{\min}, a^{\max}]$ (the interval of possible strain values), are the only influential parameters

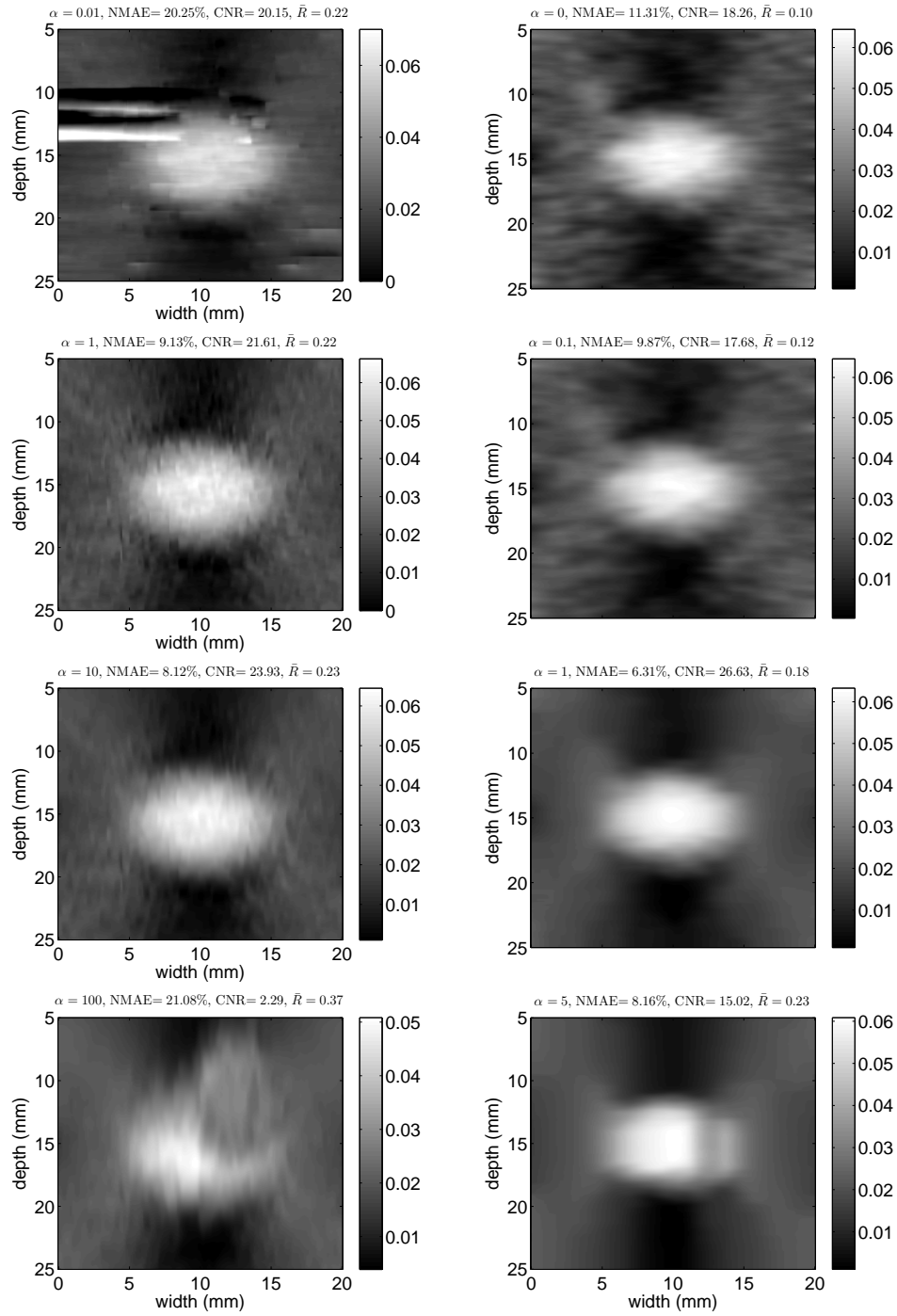Figure 3.5: A visual presentation of the result of changing the regularization parameter on the performance of the DPAM (second column) and 1D SHORTCUT(first column) methods applied to the simulation phantom data
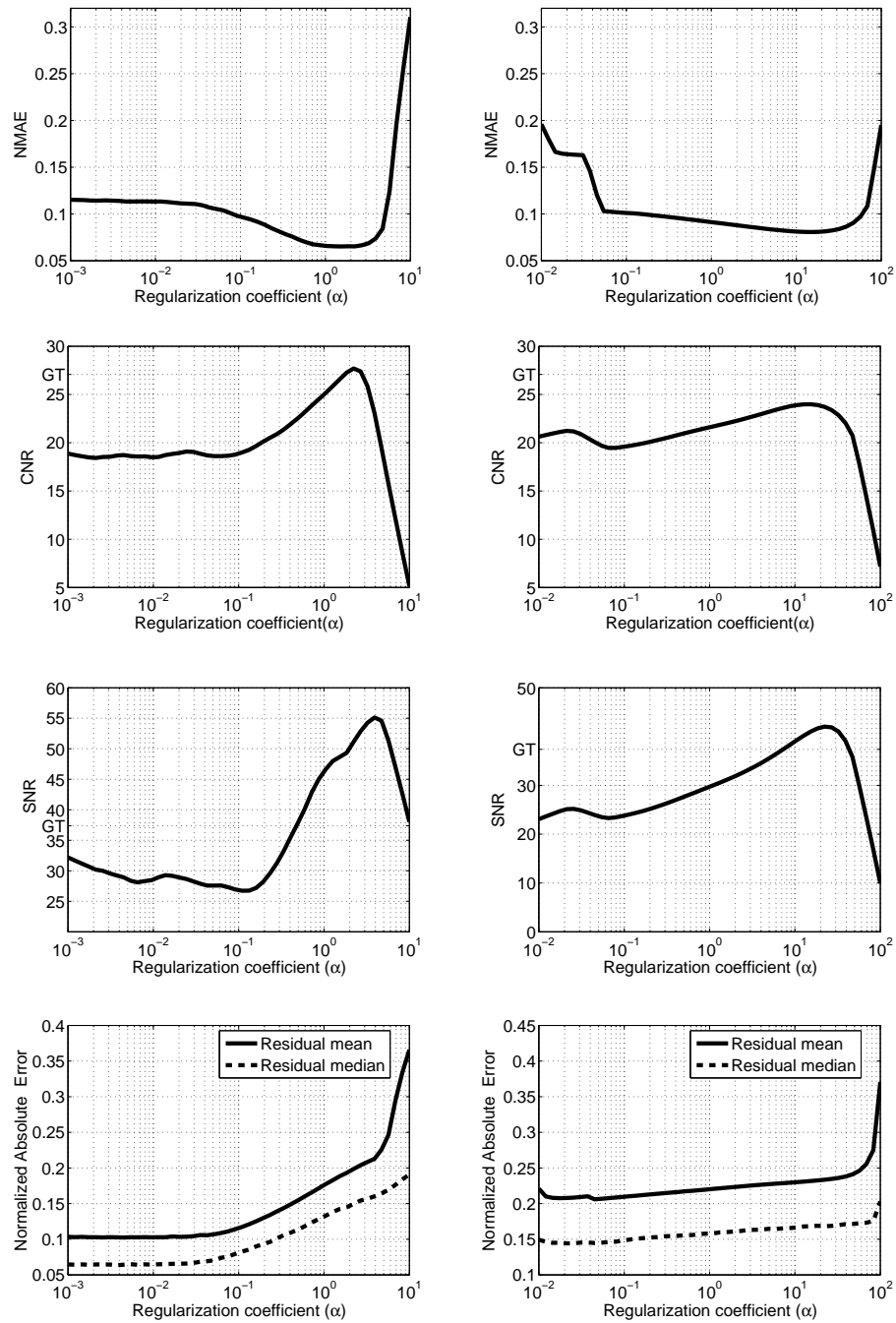
Figure 3.6: The result of changing the regularization parameter on the performance of the DPAM(second column) and 1D SHORTCUT(first column) methods applied to the simulation phantom data

of the proposed algorithm. Figure 3.5 depicts the strain image produced by DPAM and 1D SHORTCUT with different regularization coefficients. The surprising result of this analysis was that the proposed algorithm can produce fairly impressive strain image quality with $CNR = 18.26$ and $NMAE = 11.31\%$ even when the regularization parameter is set to zero. This due to the fact that since DP in SHORTCUT only searches in the domain of continuous piecewise linear displacement functions, the problem is no longer ill-posed and does not need regularization. In other words, motion continuity (the regularization term in eq. (3.3)) is already preserved by constraining the global search in the domain of continuous piecewise linear displacement functions. This is not true for the DPAM which fail at small regularization coefficients. A more clear picture arise when the performance measures are compared over a big regularization parameter span in Figure 3.6. This figure highlights shortcomings of DPAM at low regularization weights and lack thereof in 1D SHORTCUT.

3.5   Experimental Results

For experimental evaluation, RF data is acquired from an Antares Siemens system (Issaquah,WA) at the center frequency of $6.67MHz$ with a VF10-5 linear array at a sampling rate of $40MHz$ at Johns Hopkins University. In this section, phantom results and patient trials of both SHORTCUT and DPAM methods are presented and compared.

(a)

(b)
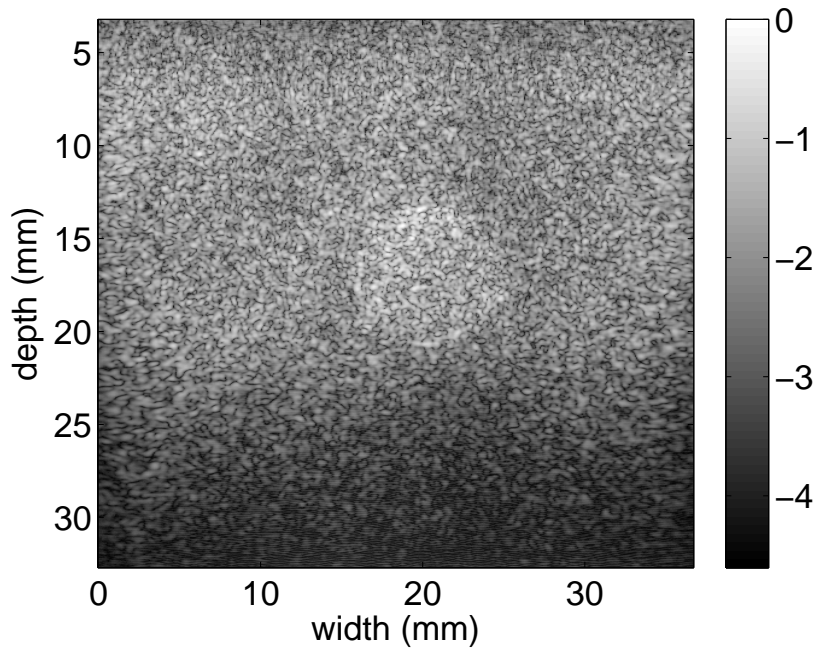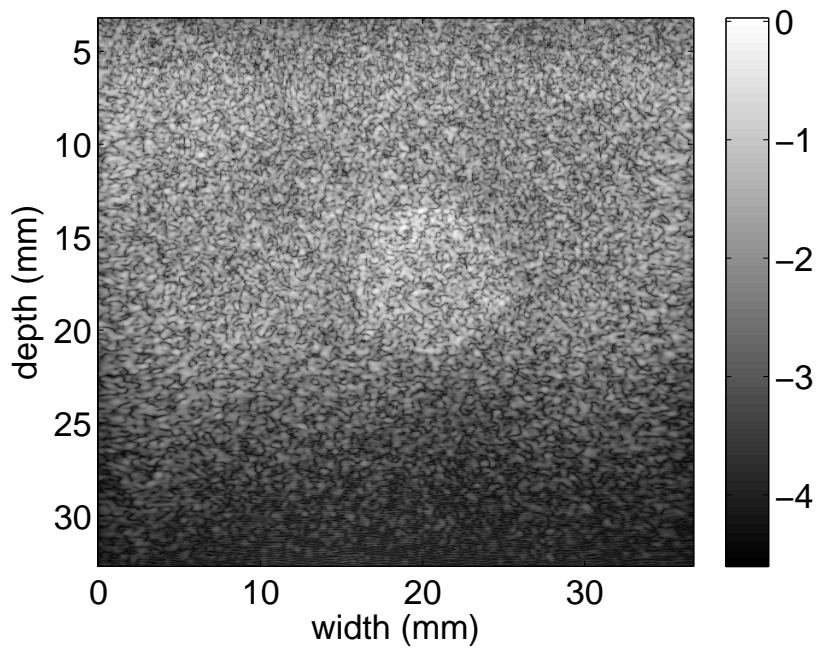
Figure 3.7: Eperimental Phantom B-Mode (a) Pre-Compression (b) Post-Compression

Table 3.2: The SNR and CNR of the strain images of the experimental phantom. target and background windows used for CNR calculation are shown in Figure 3.8. The SNR is calculated for the background window.

Method	SNR	CNR	Residual Mean	Residual Median
DPAM	51.22	6.28	0.56	0.41
SHORTCUT	483.7	101.96	0.26	0.20
Improvement Percentage	844.3%	1523.56%	53.6%	51.2%

3.5.1 Phantom Results

An elastography phantom (CIRS elastography phantom, Norfolk, VA) is compressed 0.2 inch axially using a linear stage, resulting in an average strain of 2%. The Young's elasticity modulus of the background and the lesion under compression are respectively $33kPa$ and $56kPa$. Two RF frames are acquired corresponding to before and after the compression which are depicted in Fig 3.7(a)-(b). The axial strain is calculated using both 1D SHORTCUT and DPAM methods. Fig. 3.8(a)-(d) shows the axial strain and lateral displacement maps. These results confirms that the SHORTCUT algorithm can produce smooth images without compromising the edges. Table 3.2 shows very large improvement in the SNR (844.3%) and CNR (1523.56%) of the strain maps produced by 1D SHORTCUT compared to DPAM. The lack of visible structure of 1D SHORTCUT residual compare to DPAM residual image in the last row of Figure 3.8 together with the huge improvement in residual mean (53.6%) and median (51.2%) confirms that the global optimization worth the extra computation time.

Since the phantom data contains a known lesion which produce distinct edge in the
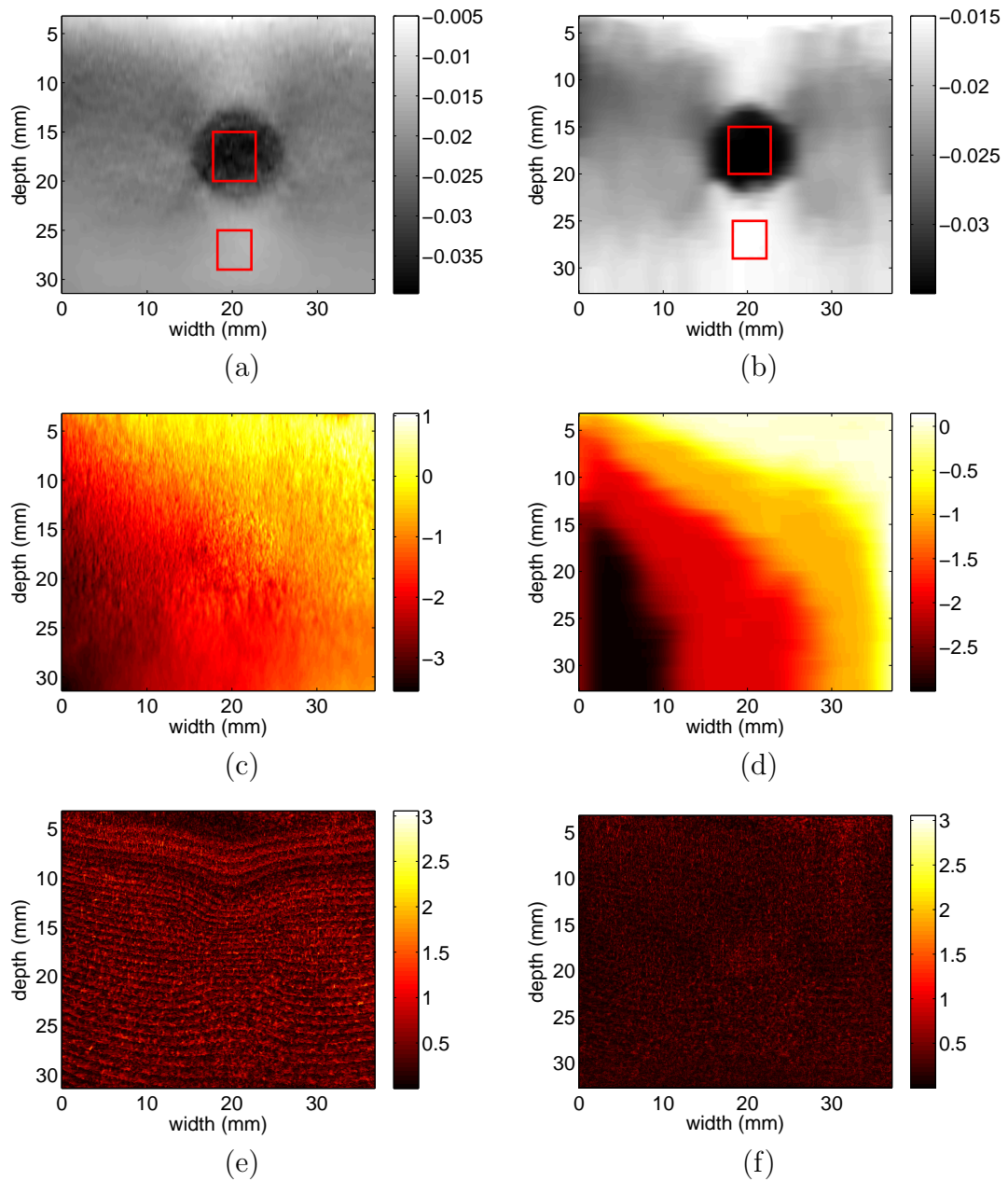
Figure 3.8: The result of different methods (first column DPAM and second column 1D SHORTCUT) applied to the phantom data: (a) Axial strain of the DPAM approach (b) Axial strain of the SHORTCUT approach (c) Lateral displacement of the DPAM approach (d) Lateral displacement of SHORTCUT approach (e) Logarithm of absolute residual in DPAM (f) Logarithm of absolute residual in SHORTCUT

strain field, it can be used to find the spatial resolution using modulation transfer function (MTF). Modulation Transfer function is an established method for estimating the spatial resolution of medical imaging systems that was relatively recently extended to elastography [49]. The spatial resolution of the reconstructed images is determined with a three-step approach [50, 51]. First, the edge spread function is computed by averaging the pixel values across the background-inclusion interface. Second, the line spread function (LSF) is computed by differentiating the edge spread function. Third, the MTF is determined by computing the Fourier transform of the LSF and normalizing the resulting function to zero spatial frequency

$$MTF(k) = \frac{\Xi(k)}{\Xi(0)}.$$ (3.17)

This measure along with CNR, SNR, residual mean and residual median will be used in this section to assess the effect of different number of strain discretization N and regularization α. For the DPAM method, the effect of regularization on the residuals have been assessed and it has been shown that adding the regularization term will eliminate many of the local minima and makes the displacement field smooth, a generally desired attribute. However, since SHORTCUT is a global optimization approach, the convexity and local minima of the cost function is of no concern. As it was showed in the previous section, the SHORTCUT algorithm can produce acceptable performance measures even with zero α.

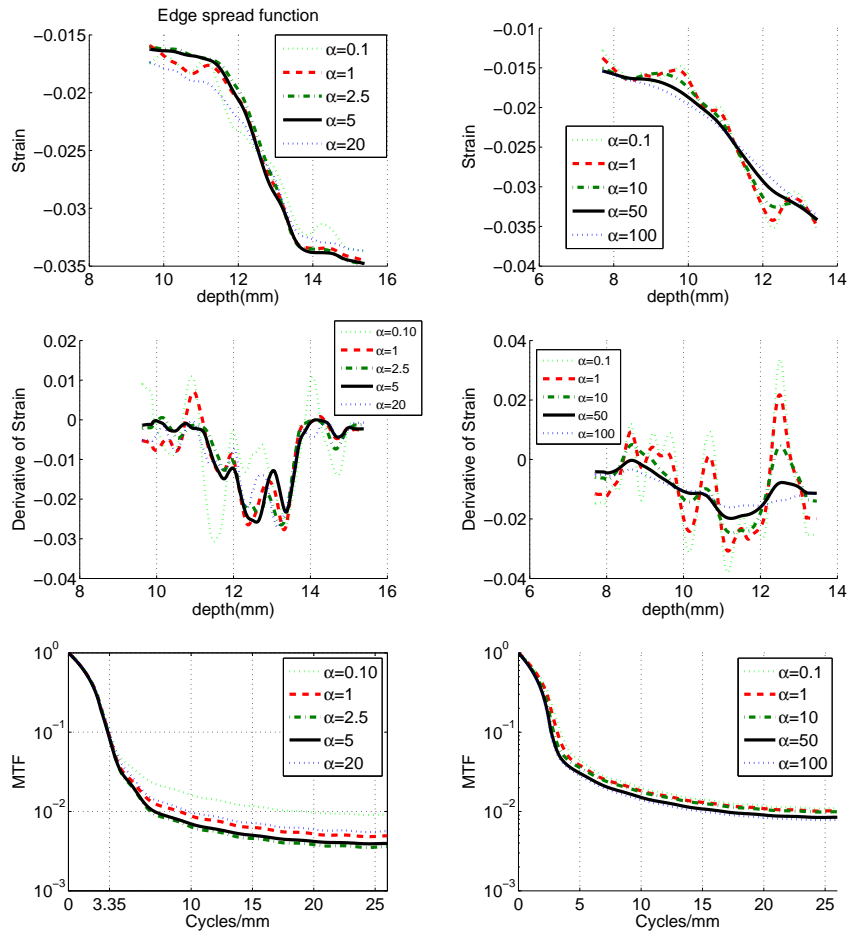Figure 3.9: The effect of changing the regularization α on the ESF, LSF and MTF (spatial resolution) when different methods applied to the phantom data. The first column is the result of 1D SHORTCUTP and the second column is the result of DPAM.

The effect of changing the regularization weight

The simulation data analysis on the effect of changing the regularization parameter α_a in eq. (3.6) on the performance of the proposed 1D SHORTCUT is repeated here on the phantom data. As stated earlier, the existence of a distinct edge in the phantom data make the measurement of the spatial resolution possible. Figure 3.9 compares the ESF, LSF and MTF of both DPAM and 1D SHORTCUT and it shows that the edge is much sharper in the proposed method overall and at high regularization parameters, the edges are not smoothed out DPAM. Figure 3.11 depicts the strain image produced by DPAM and 1D SHORTCUT with different regularization coefficients. Here also the proposed algorithm can produce impressive strain image quality with $CNR = 13.44$ and $SNR = 25.68$ even when the regularization parameter is set to zero. This is not true for the DPAM which fail at small regularization coefficients. A more clear picture arise when the performance measures are compared over a big regularization parameter span in Figure 3.10. This figure confirms the failing of DPAM at low regularization parameter and lack thereof in 1D SHORTCUT. The last row of this figure shows that the proposed algorithm achieved the global minimum of the residual which is substantially better compared to DPAM.

The effect of number of strain discretization

The regularization coefficient together with N which determine the number of discretizes strain values sampled uniformly from the interval $[a^{\min}, a^{\max}]$ (the interval of possible strain values), are the only parameters of the proposed algorithm. In this
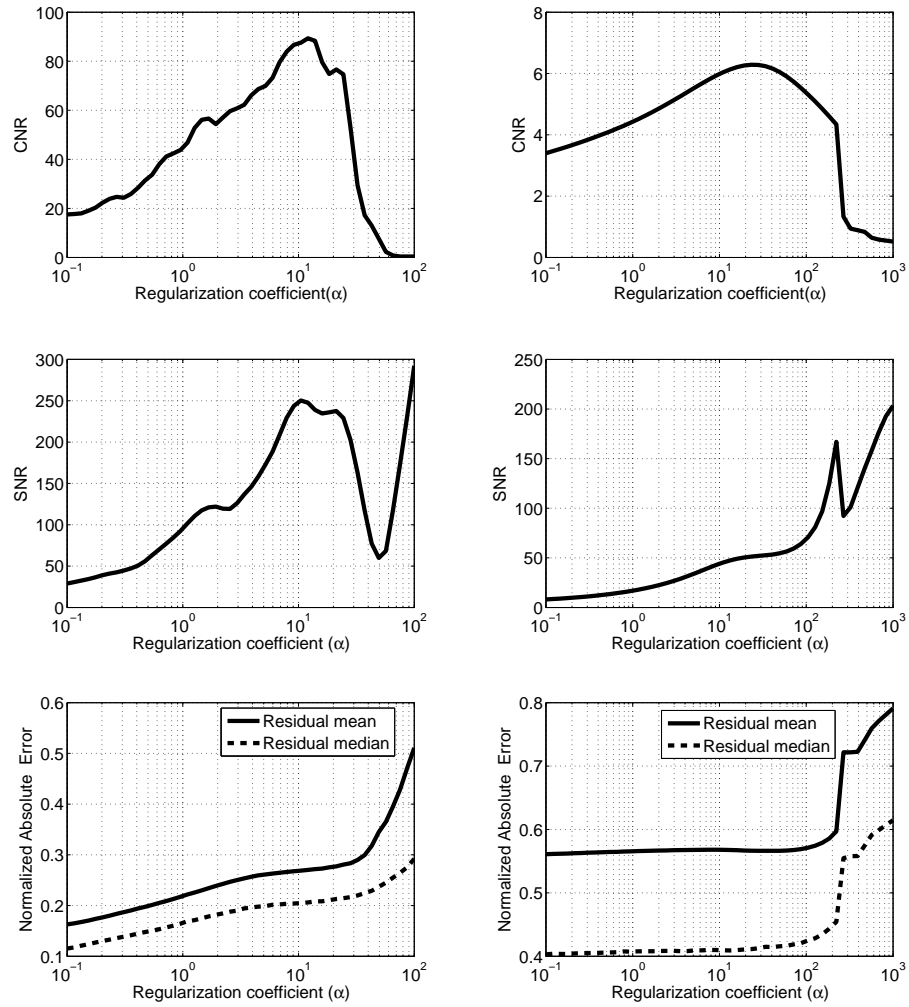
Figure 3.10: The effect of changing the regularization α on the CNR, SNR and residual mean and median when different methods applied to the phantom data. The first column is the result of 1D SHORTCUT and the second column is the result of DPAM
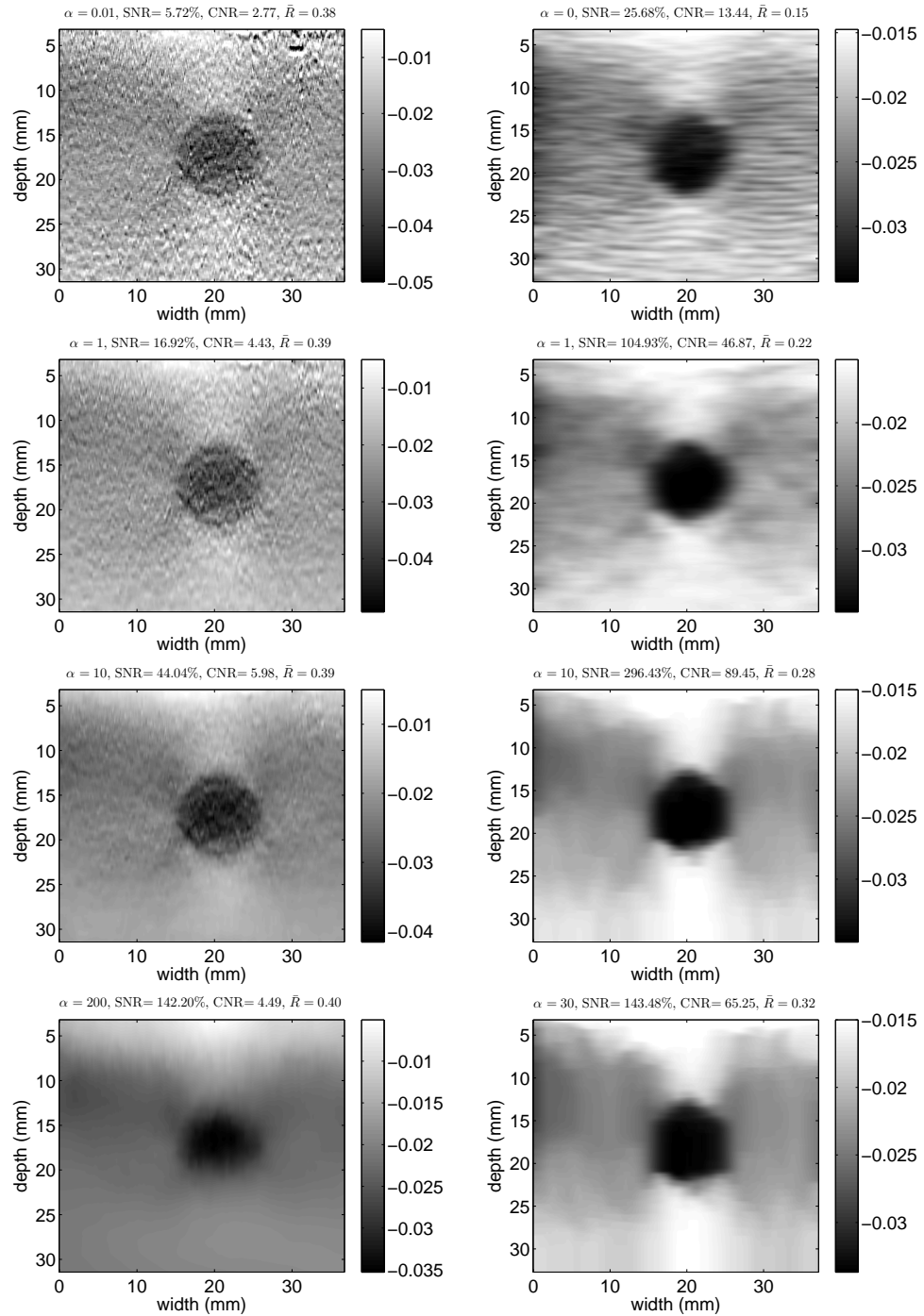
Figure 3.11: A visual presentation of the result of changing the regularization parameter on the performance of the DPAM (second column) and 1D SHORTCUT(first column) methods applied to the experimental phantom data

part, the effect of changing the number of strain discretization N on the performance of the 1D SHORTCUT is assessed. Figure 3.12 represents the MTF, CNR, SNR and other performance measures when N sweep from only two strain levels (in this mode SHORTCUT produces black and white strain image and can be used for classification) to 100 levels. In terms of spatial resolution, the performance of the algorithm is almost stable. However at lower number of strain levels the CNR, SNR and residual mean and median is not good. at these numbers, substantially better performance can be achieved when α is modified accordingly (in this study the α is assumed to be constant at $\alpha = 7.8$). Since with Lower N the jumps of the strain is higher therefore one needs bigger α to produce high quality strain images. Generally speaking higher N will result in lower residual error. Figure 3.13 shows axial strain image for different N which shows that given a fix α higher N will result in smoother but almost equally sharp images. The proposed algorithm was tested on a desktop with Intel Core i7 3.4 GHz CPU. Figure 3.14 shows the computation time of this algorithm with different N when the number of lateral displacement levels is $M = 10$. This figure shows that the computation time grows linearly with the N. The same relationship holds for M since the total computation is in order of $\mathcal{O}(3 \times N \times M \times n \times m)$

3.5.2 Clinical Study: in-vivo data

The *In-vivo* data is acquired from five patients undergoing open surgical radiofrequency thermal ablation for primary or secondary liver cancers. This data is collected as follows at Johns Hopkins Hospital: for the first patient, ultrasound RF data

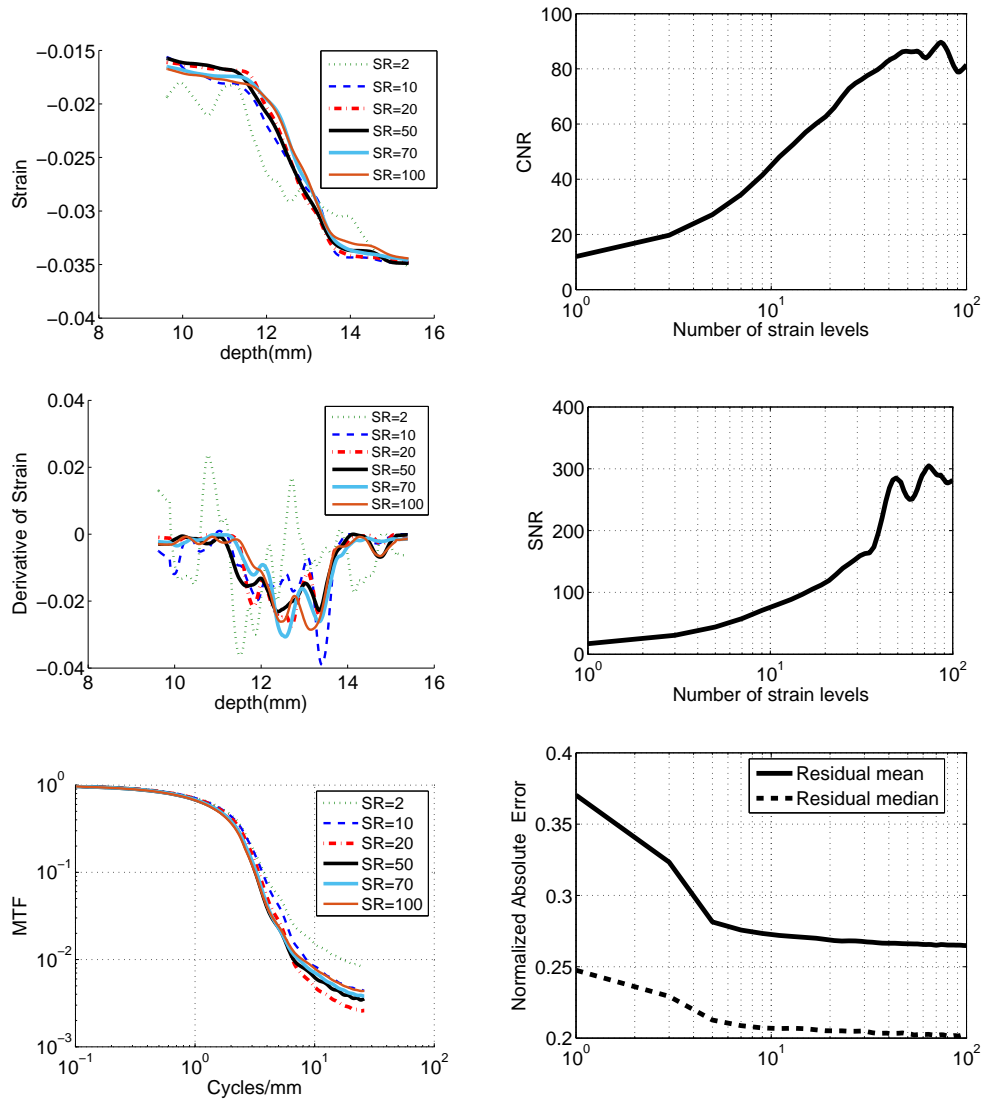Figure 3.12: The effect of choosing different number of strain discretization N on the performance measures applied to phantom data
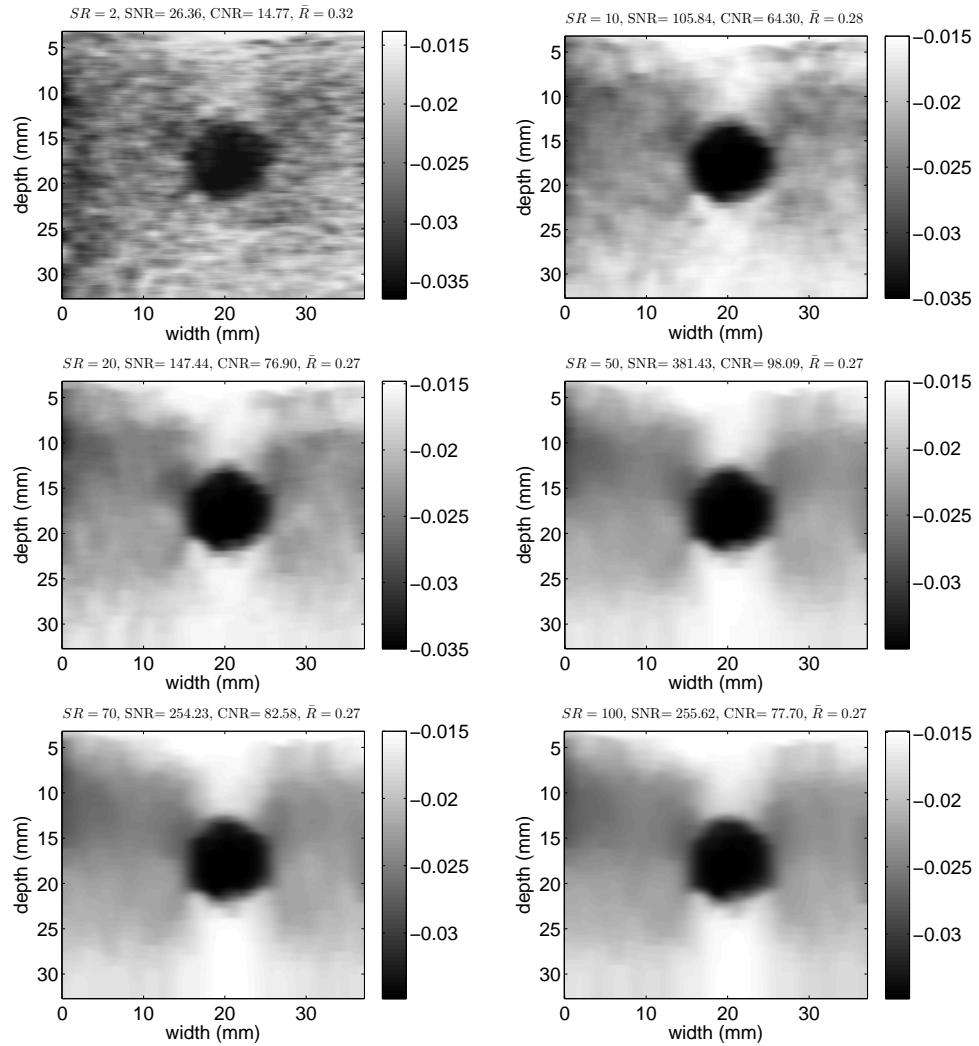
Figure 3.13: Effect of different number of strain discretization N on the qualitative features of the strain images produced by 1D SHORTCUT.
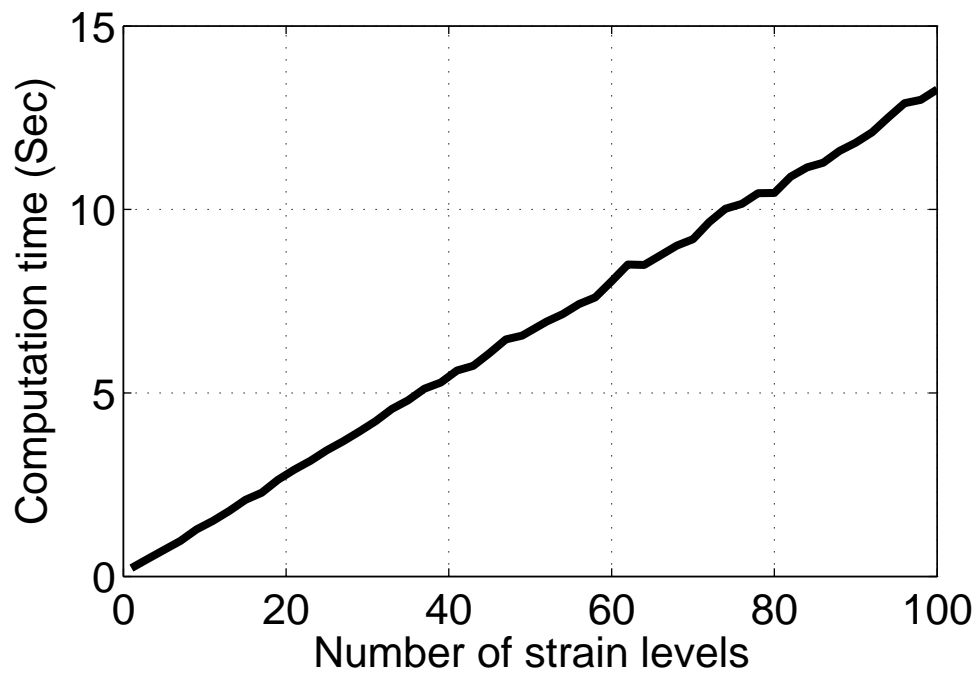
Figure 3.14: Computation time for different number of axial strain levels N when the numbe of lateral displacement levels are fixed at $M = 10$.

is acquired only after ablation. For the second, third, and fourth patients, ultrasound RF data is collected both before and after ablation. Data collection from the tumour involved holding the probe is hard-to-reach locations and angles, which lead to unwanted out-of-plane motions of the probe. In addition, micro-bubbles and high temperature gradients created by the ablation process add noise in the the RF data. Furthermore, the pulsation of hepatic vessels create complicated deformation fields. Therefore, the pre- and post-compression images suffer from high levels of decorrelation.

Figures 3.15, 3.17, 3.19, 3.21, 3.23 depict the pre- and post-compression B-mode image of the five patients. Figures 3.16, 3.18, 3.20, 3.22, 3.24 compare the axial strain images, lateral displacement images and residual images of the 2D SHORTCUT with DPAM. In all of the axial strain images of different patients, the 2D SHORTCUT outperforms the DPAM in terms of CNR and SNR specially in the upper and lower quarter of the image which is over-smoothed in DPAM. This can also be confirmed in Tables 3.3, 3.4, 3.5, 3.6, 3.7 where large improvements in terms of CNR, SNR, residual mean and residual median are evident. Although DPAM has failed on some local regions, the proposed 2D SHORTCUT has been able to find the global optimal solution and has not been failed. Notice that the dynamic range of strain variation in SHORTCUT is much higher than DPAM. This is especially more recognizable in Figure 3.22 and Figure 3.24 where from the same RF data SHORTCUT produced strains as high as 0.03 and 0.03 compare to 0.02 and 0.015 in DPAM. This can be justified by the fact that the SHORTCUT algorithm does not penalize higher strain

Table 3.3: The patient 1 results of DPAM and SHORTCUT approach are compared in terms of SNR, CNR, residual mean, residual median. Target and background windows used for CNR calculation are shown in Figure 3.16.

Method	SNR	CNR	Residual Mean	Residual Median
DPAM	5.35	3.87	0.67	0.47
SHORTCUT	25.55	23.27	0.586	0.397
Improvement Percentage	433.6%	501.3%	12.5%	17%

Table 3.4: The patient 2 results of DPAM and SHORTCUT approach are compared in terms of SNR, CNR, residual mean, residual median. Target and background windows used for CNR calculation are shown in Figure 3.18.

Method	SNR	CNR	Residual Mean	Residual Median
DPAM	2.66	2.60	0.637	0.45
SHORTCUT	17	19.48	0.562	0.415
Improvement Percentage	539%	649.2%	11.8%	7.8%

Table 3.5: The patient 3 results of DPAM and SHORTCUT approach are compared in terms of SNR, CNR, residual mean, residual median. Target and background windows used for CNR calculation are shown in Figure 3.20.

| Method	SNR	CNR	Residual Mean	Residual Median
DPAM	10.5	13.18	0.596	0.432
SHORTCUT	44.48	60.09	0.497	0.339
Improvement Percentage	323.6%	355.9%	16.6%	21.52%

Table 3.6: The patient 4 results of DPAM and SHORTCUT approach are compared in terms of SNR, CNR, residual mean, residual median. Target and background windows used for CNR calculation are shown in Figure 3.22.

Method	SNR	CNR	Residual Mean	Residual Median
DPAM	1.872	0.328	0.5482	0.3913
SHORTCUT	15.94	22.53	0.372	0.242
Improvement Percentage	751.5%	6768.9%	32.14%	38.15%

value eq. (3.6) as it is the case in DPAM eq. (3.3), it regularizes the derivative of the strain i.e. the tissue change is regularized. In order to better visualize results in these two patient pink color scale is used instead of gray scale.
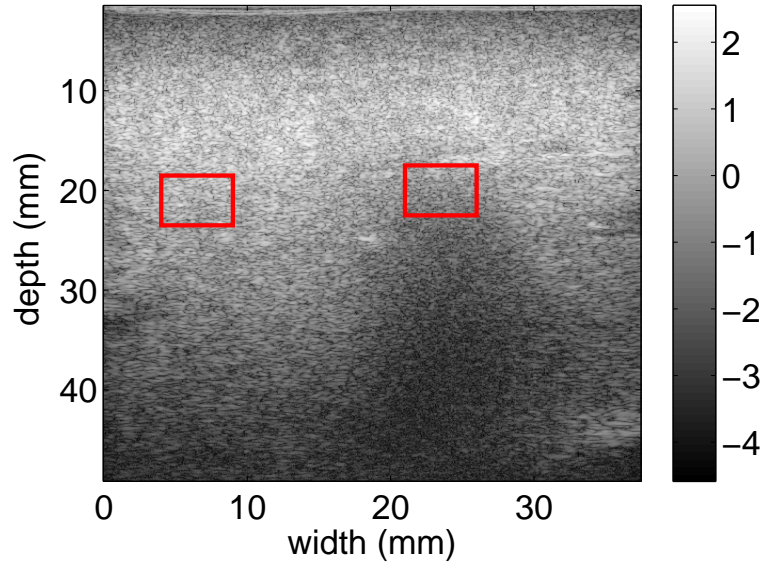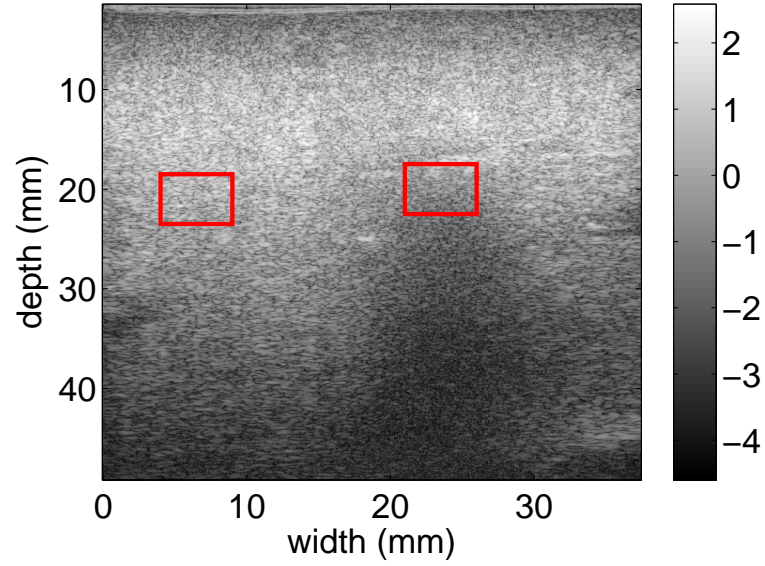
Figure 3.15: Clinical Study patient 1 B-Mode images (a) Pre-Compression (b) Post-Compression

Figure 3.16: The result of different methods (first column 2D SHORTCUT and second column DPAM) applied to the patient 1: (a) Axial strain of the 2D SHORTCUT approach (b) Axial strain of the DPAM approach c) Lateral displacement of the 2D SHORTCUT approach (d) Lateral displacement of DPAM approach (e) Logarithm of absolute residual in 2D SHORTCUT (f) Logarithm of absolute residual in DPAM

Figure 3.17: Clinical Study patient 2 B-Mode images (a) Pre-Compression (b) Post-Compression
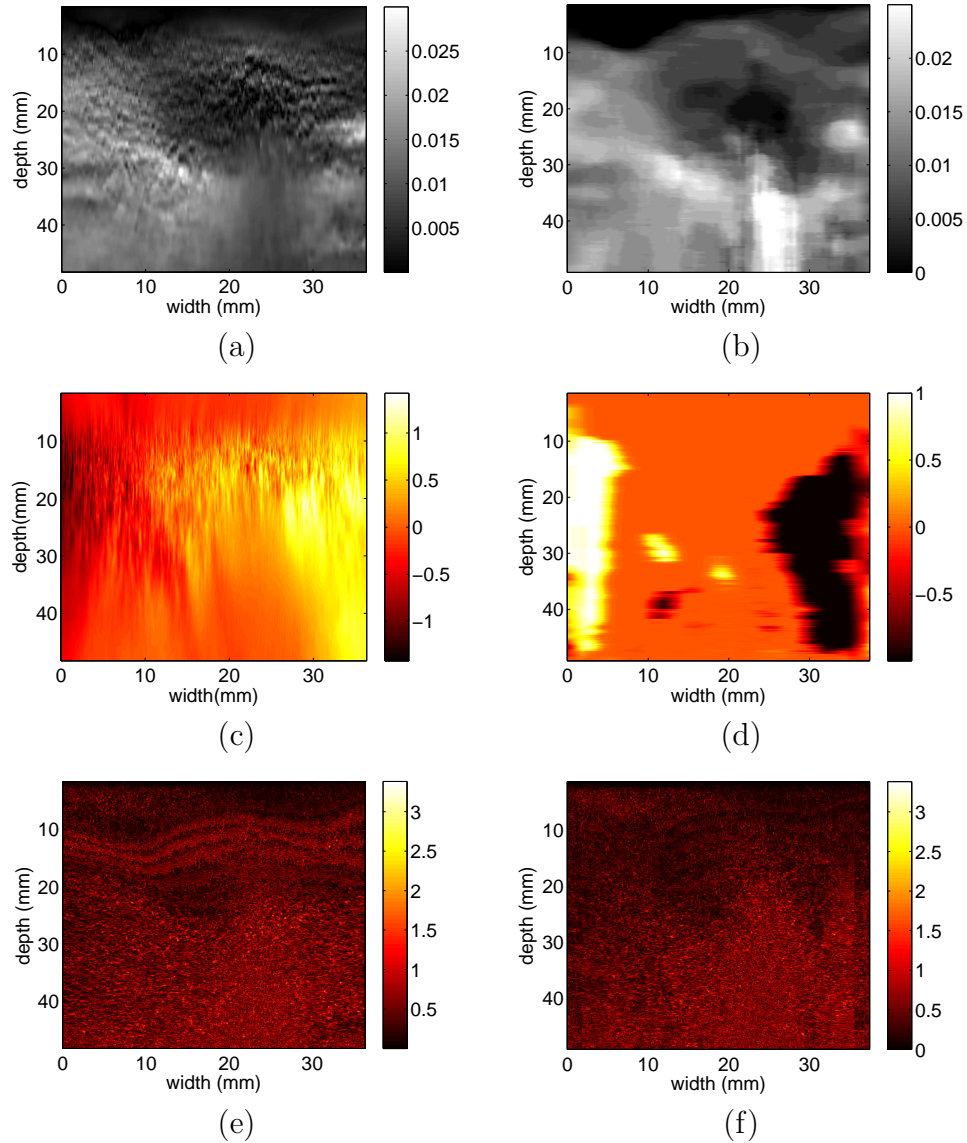
Figure 3.18: The result of different methods (first column 2D SHORTCUT and second column DPAM) applied to the patient 2: (a) Axial strain of the 2D SHORTCUT approach (b) Axial strain of the DPAM approach (c) Lateral displacement of the 2D SHORTCUT approach (d) Lateral displacement of DPAM approach (e) Logarithm of absolute residual in 2D SHORTCUT (f) Logarithm of absolute residual in DPAM

Figure 3.19: Clinical Study patient 3 B-Mode images (a) Pre-Compression (b) Post-Compression

Figure 3.20: The result of different methods (first column 2D SHORTCUT and second column DPAM) applied to the patient 3: (a) Axial strain of the 2D SHORT-CUT approach (b) Axial strain of the DPAM approach (c) Lateral displacement of the 2D GDP approach (d) Lateral displacement of DPAM approach (e) Logarithm of absolute residual in 2D SHORTCUT (f) Logarithm of absolute residual in DPAM
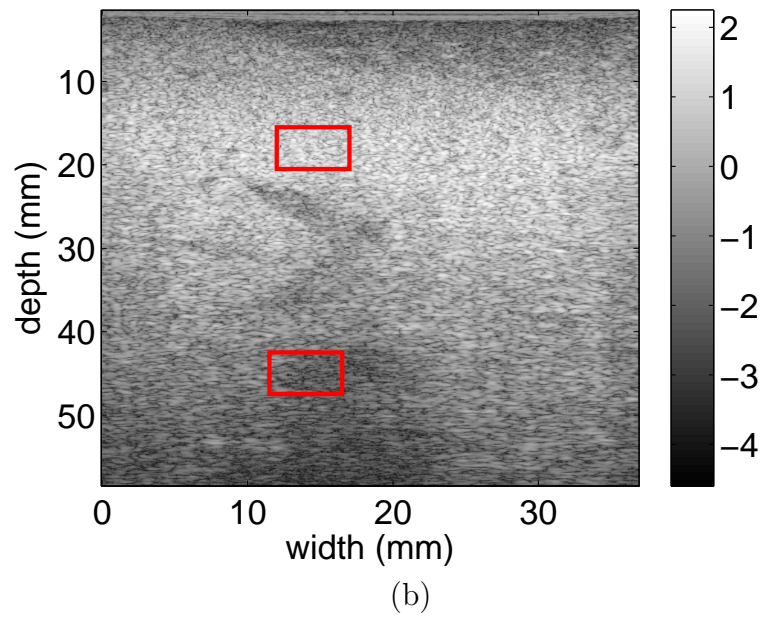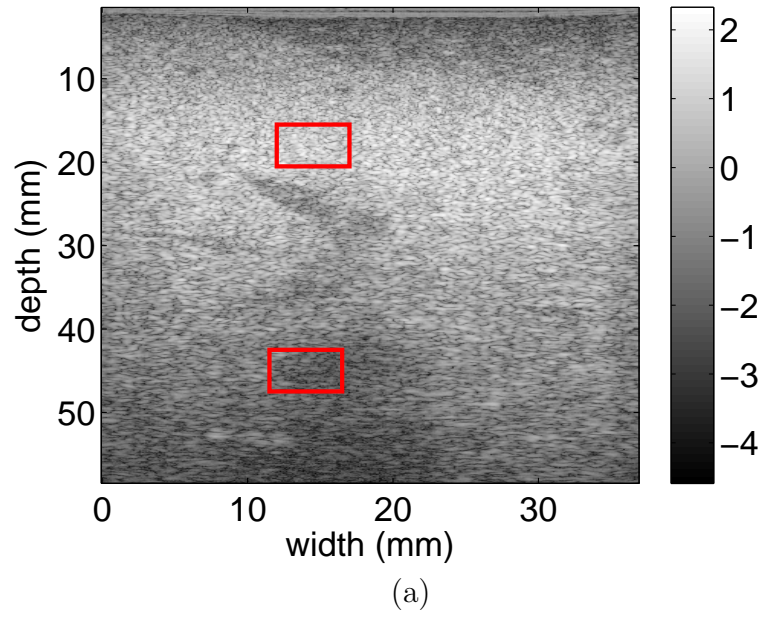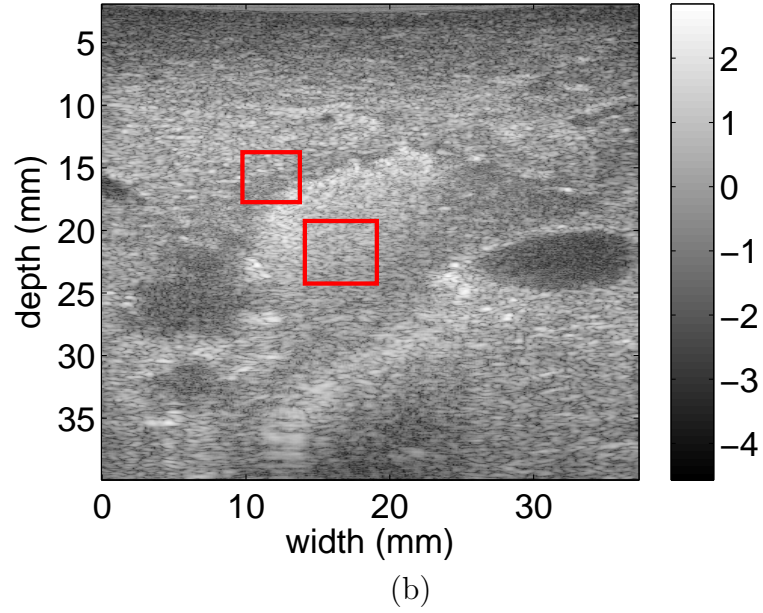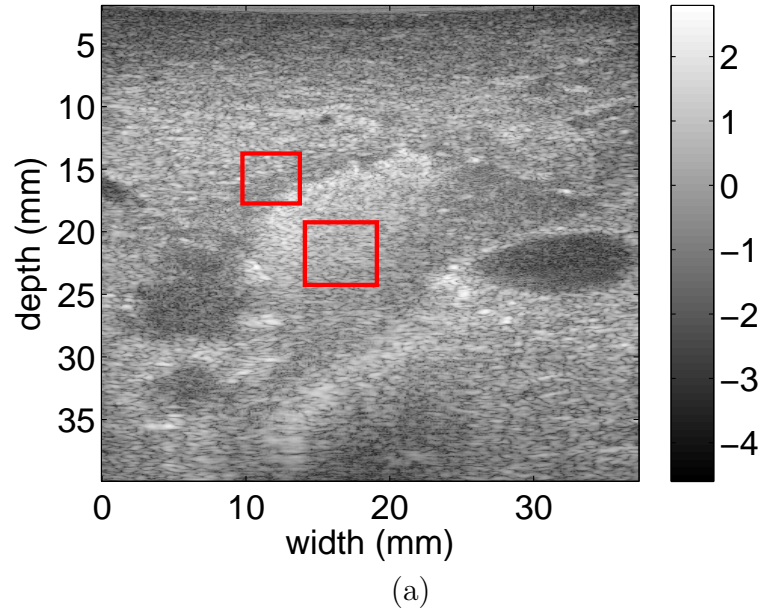
Figure 3.21: Clinical Study patient 2 B-Mode images (a) Pre-Compression (b) Post-Compression
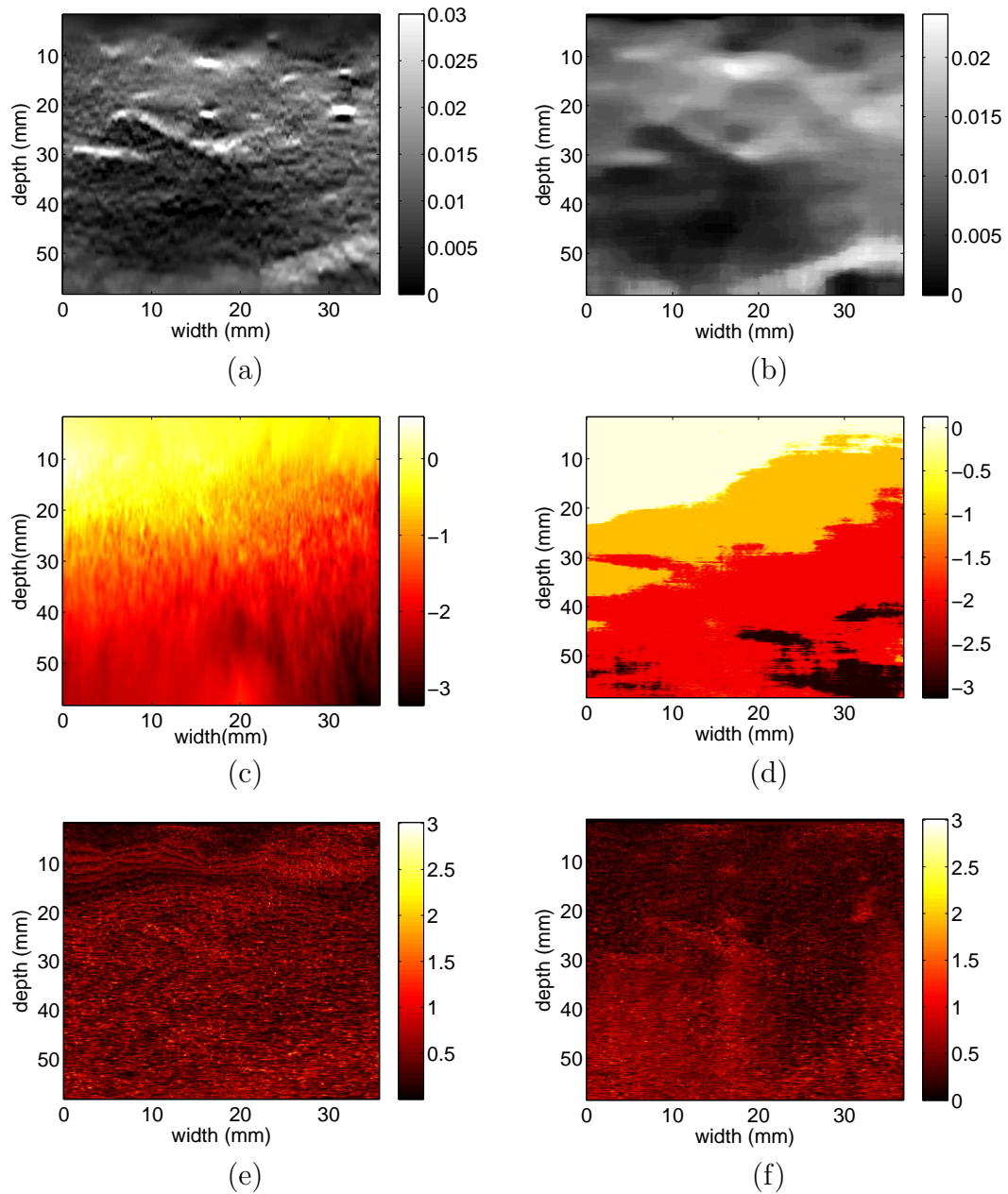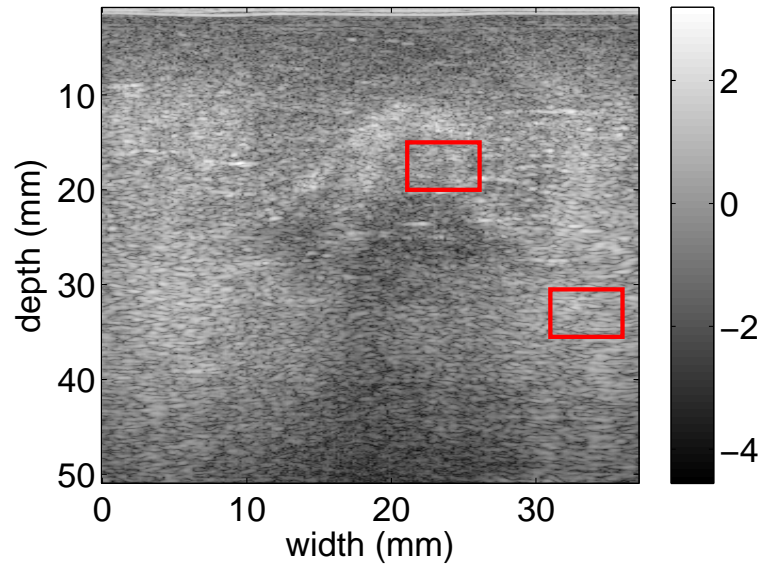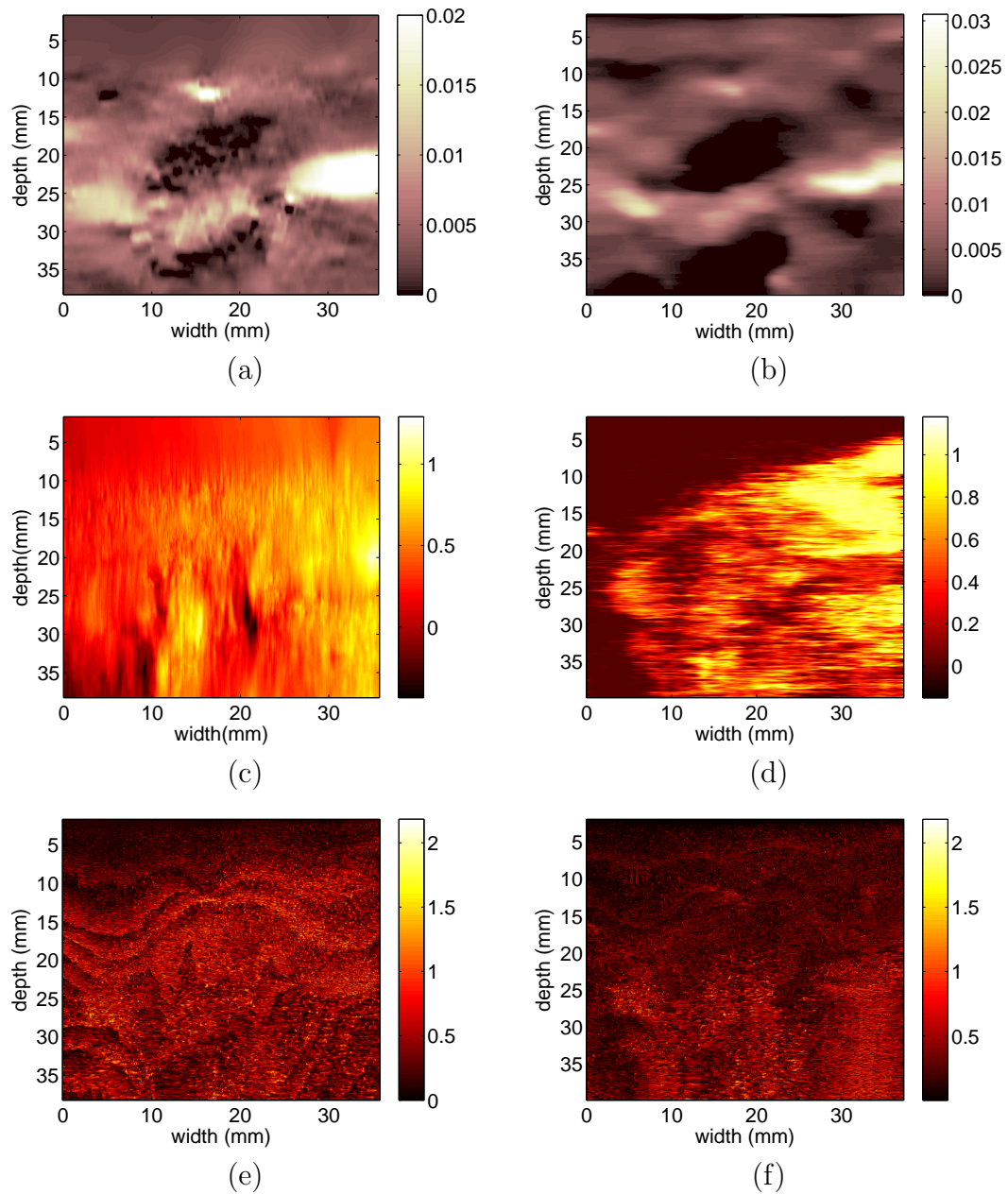
Figure 3.22: The result of different methods (first column 2D SHORTCUT and second column DPAM) applied to the patient 4: (a) Axial strain of the 2D SHORTCUT approach (b) Axial strain of the DPAM approach (c) Lateral displacement of the 2D SHORTCUT approach (d) Lateral displacement of DPAM approach (e) Logarithm of absolute residual in 2D SHORTCUT (f) Logarithm of absolute residual in DPAM.
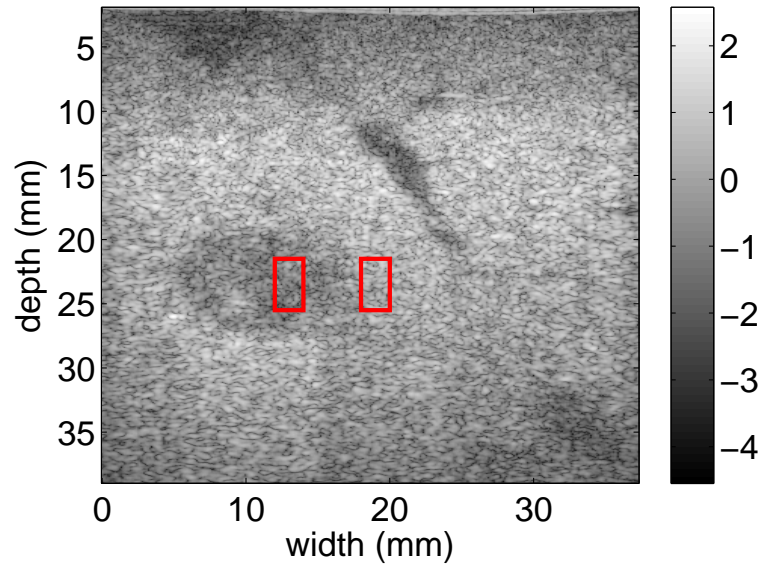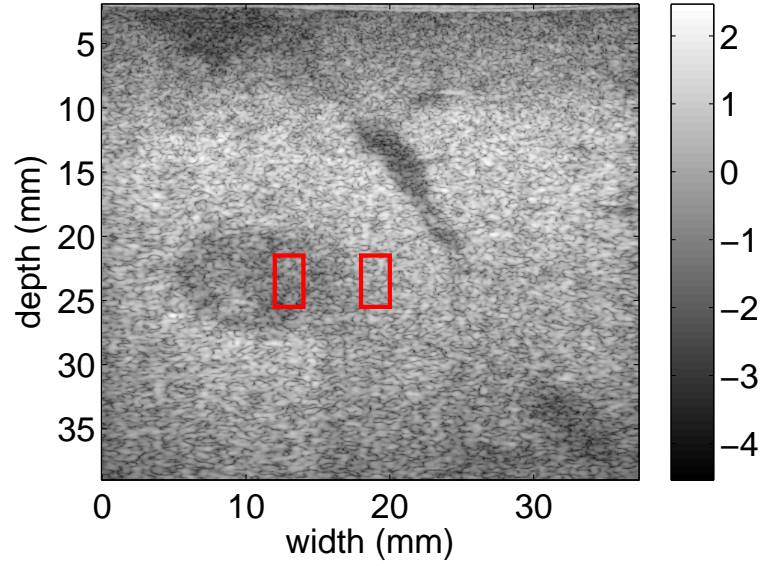
Figure 3.23: Clinical Study patient 5 B-Mode images (a) Pre-Compression (b) Post-Compression
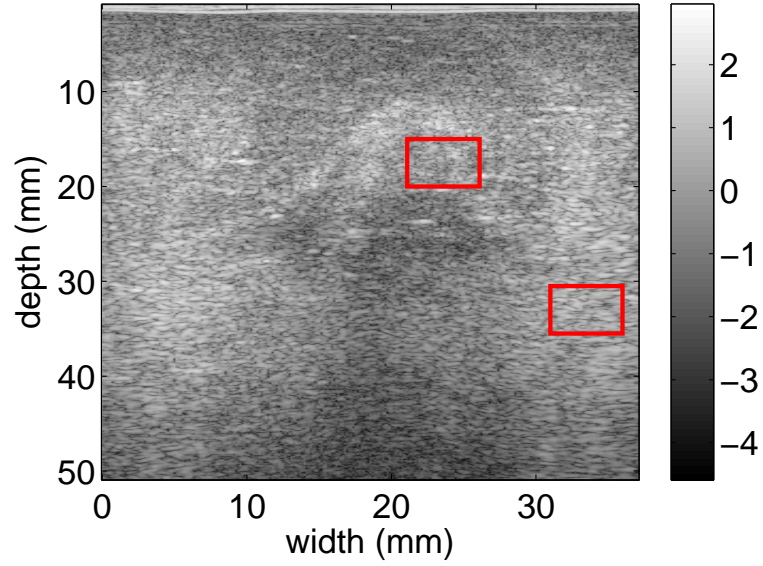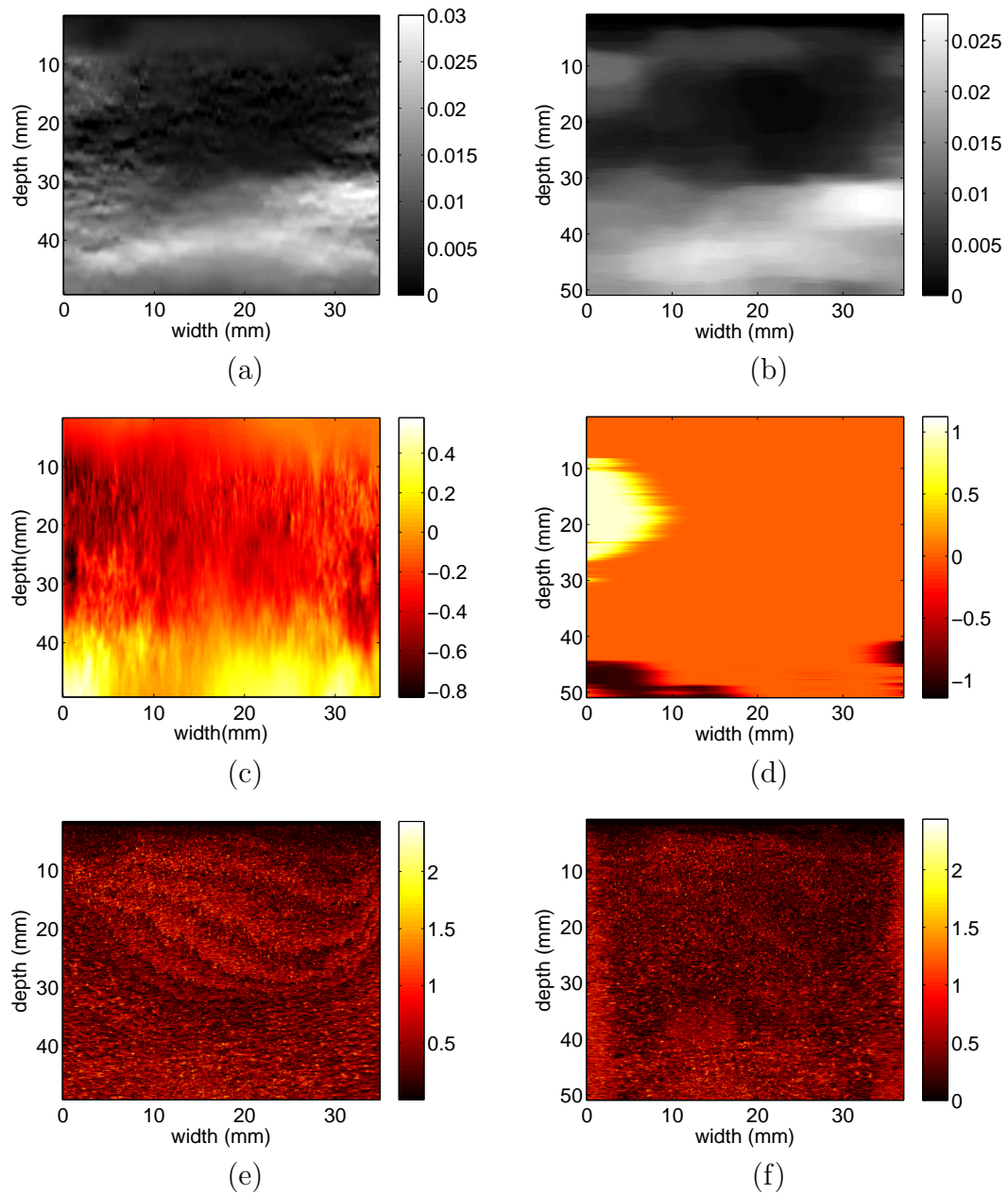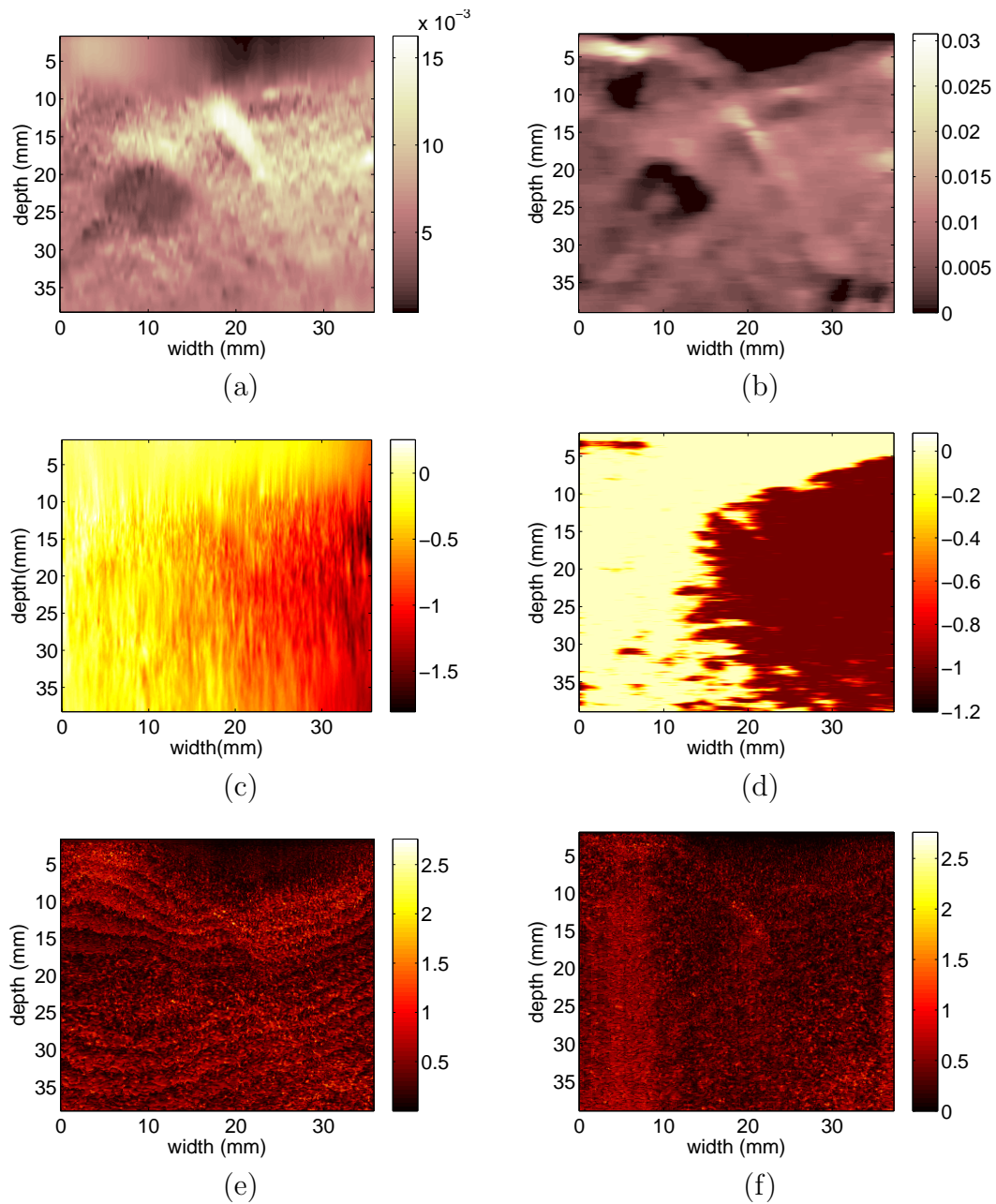
Figure 3.24: The result of different methods (first column 2D SHORTCUT and second column DPAM) applied to the patient 5: (a) Axial strain of the 2D SHORTCUT approach (b) Axial strain of the DPAM approach (c) Lateral displacement of the 2D SHORTCUT approach (d) Lateral displacement of DPAM approach (e) Logarithm of absolute residual in 2D SHORTCUT (f) Logarithm of absolute residual in DPAM

Table 3.7: The patient 5 results of DPAM and SHORTCUT approach are compared in terms of SNR, CNR, residual mean, residual median. Target and background windows used for CNR calculation are shown in Figure 3.22.

Method	SNR	CNR	Residual Mean	Residual Median
DPAM	6.81	3.03	0.5592	0.4014
SHORTCUT	20.75	26.23	0.4572	0.2956
Improvement Percentage	204.7%	765.7%	18.25%	26.35%

Chapter 4

Conclusions and Future Work

4.1   Conclusions

In the first chapter of this thesis, we have presented an algorithm that can, under certain assumptions, generate strain images with uniform precision but varying resolution. Uniform precision property ensures that textures/variations in the strain image reflect underlying tissue properties and are not caused by errors in the displacement estimation. The algorithm has also the capability of keeping the edges between different tissue structures sharp while minimizing the noise. This is demonstrated by the phantom and *in-vivo* clinical data. The results are compared to three common methods in this field which showed the effectiveness of the proposed algorithm, however, further clinical studies will be necessary to assess the benefits of the algorithm.

The second chapter of this thesis introduces a 2-D strain imaging technique called

SHORTCUT (meSHing Of gRadienT in DP for direCt Ultrasound elasTography). The proposed technique is simple, fast, robust and accurate and it directly produces the strain images from RF data using a novel dynamic programming (DP) technique. Unlike the standard DP algorithm which discretizes the decision space (displacement field) and search in the space of piecewise constant functions, the proposed DP discretizes the gradient of the decision space (strain field) and search the space of continuous piecewise linear functions. The proposed algorithm results in substantial improvement in SNR, CNR and accuracy of the estimations. This is mainly the consequence of three major paradigm shifts compared to the available strain estimation techniques in the literature:

- Eliminating the displacement differentiation block,

- penalizing the tissue discontinuity instead of strain values,

- performing a global search rather than local search.

The robustness of this method emanates from the fact that DP is global optimization algorithm, therefore not only its accurate in the sense that it always finds the globally optimal estimations but also it can only be locally affected by signal decorrelation. To further improve the results, a 2D version of SHORTCUT was also introduced which utilizes a special bilateral filter. The effectiveness of the proposed method is investigated through simulation data, phantom experiments, and *in vivo* patient data. The results are compared with previous work called DPAM which confirms the merits of this approach. Given different initial settings this method can operates somewhere

between a few milliseconds to a few seconds and is thus also potentially suitable for real time elastography. It is also worth mentioning that this method is compatible with parallel computing which can drastically decrease the computation time when multiple processors are available.

4.2 Future Work

There are several ways that this algorithm can be improved or altered for a specific application. We list the possible future work as follow:

- Speed of this algorithm can be significantly increased by an adaptive compromise between global and local search in DP. One idea could be that once the problem is solved for an axial line the information of this solution can bound the search domain of the neighboring axial lines.

- There also exists numerous algorithms for reducing the computational burden of DP without prior information such as branch and bound algorithm in which unnecessary branches are eliminated from the search. Nearly all of these algorithms need a trade-off between the global and local search.

- This algorithm can be coupled with an inverse problem formulation to calculate the elasticity modulus.

- Results may be improved by solving a 2D DP which is formulated by defining a tree that connects all the pixels in the RF data.

- Since this algorithm can produce strain images with any number of strain levels, it can be used for classification of different tissues.

- Finally, a temporal filter of the like discussed in the third section of chapter three can also be added to evoke the extra information maintained in the successive RF data.

Bibliography

[1] R. F. Wagner, S. W. Smith, J. M. Sandrik, and H. Lopez, "Statistics of speckle in ultrasound b-scans," *IEEE Transactions on sonics and ultrasonics*, vol. 30, no. 3, pp. 156–163, 1983.

[2] T. J. Hall, P. Barbone, A. Oberai, and et al., "Recent results in nonlinear strain and modulus imaging," *Current medical imaging reviews*, vol. 7, no. 4, 2011.

[3] O. Mohareri, A. Ruszkowski, J. Lobo, J. Ischia, A. Baghani, G. Nir, H. Eskandari, E. Jones, L. Fazli, L. Goldenberg, M. Moradi, and S. Salcudean, "Multiparametric 3d quantitative ultrasound vibro-elastography imaging for detecting palpable prostate tumors," in *MICCAI 2014*. Springer, 2014, pp. 561–568.

[4] J.-L. Gennisson, T. Deffieux, M. Fink, and M. Tanter, "Ultrasound elastography: principles and techniques," *Diagnostic and interventional imaging*, vol. 94, no. 5, pp. 487–495, 2013.

[5] G. Treece, J. Lindop, L. Chen, J. Housden, R. Prager, and A. Gee, "Real-time quasi-static ultrasound elastography," *Interface focus*, vol. 1, no. 4, pp. 540–552, 2011.

[6] R. Ahmed, R. Arfin, M. H. Rubel, K. K. Islam, C. Jia, D. Metaxas, B. S. Garra, and S. K. Alam, "Comparison of windowing effects on elastography images: Simulation, phantom and in vivo studies," *Ultrasonics*, vol. 66, pp. 140–153, 2016.

[7] H. Rivaz, E. M. Boctor, M. A. Choti, and G. D. Hager, "Real-time regularized ultrasound elastography," *Medical Imaging, IEEE Transactions on*, vol. 30, no. 4, pp. 928–945, Apr 2011.

[8] K. Parker, M. Doyley, and D. Rubens, "Corrigendum: Imaging the elastic properties of tissue: the 20 year perspective," *Physics in Medicine and Biology*, vol. 57, no. 16, p. 5359, 2012.

[9] C. Hoerig, J. Ghaboussi, and M. F. Insana, "An information-based machine learning approach to elasticity imaging," *Biomechanics and modeling in mechanobiology*, vol. 16, no. 3, pp. 805–822, 2017.

[10] S. R. Mousavi, A. Sadeghi-Naini, G. J. Czarnota, and A. Samani, "Towards clinical prostate ultrasound elastography using full inversion approach," *Medical physics*, vol. 41, no. 3, 2014.

[11] M. Tanter and M. Fink, "Ultrafast imaging in biomedical ultrasound," *IEEE transactions on ultrasonics, ferroelectrics, and frequency control*, vol. 61, no. 1, pp. 102–119, 2014.

[12] K. R. Nightingale, M. L. Palmeri, R. W. Nightingale, and G. E. Trahey, "On the feasibility of remote palpation using acoustic radiation force," *The Journal of the Acoustical Society of America*, vol. 110, no. 1, pp. 625–634, 2001.

[13] K. Nightingale, R. Bentley, and G. Trahey, "Observations of tissue response to acoustic radiation force: opportunities for imaging," *Ultrasonic imaging*, vol. 24, no. 3, pp. 129–138, 2002.

[14] M. L. Palmeri and K. R. Nightingale, "On the thermal effects associated with radiation force imaging of soft tissue," *IEEE transactions on ultrasonics, ferroelectrics, and frequency control*, vol. 51, no. 5, pp. 551–565, 2004.

[15] B. J. Fahey, M. L. Palmeri, and G. E. Trahey, "Frame rate considerations for real-time abdominal acoustic radiation force impulse imaging," *Ultrasonic imaging*, vol. 28, no. 4, pp. 193–210, 2006.

[16] L. Yuan and P. C. Pedersen, "Analytical phase-tracking-based strain estimation for ultrasound elasticity," *IEEE transactions on ultrasonics, ferroelectrics, and frequency control*, vol. 62, no. 1, pp. 185–207, 2015.

[17] J. Ophir, S. Alam, B. Garra, F. Kallel, E. Konofagou, T. Krouskop, and T. Varghese, "Elastography," *Annu. Rev. Biomed. Eng.*, vol. 213, pp. 203–233, Nov. 1999.

[18] T. J Hall, P. E Barboneg, A. A Oberai, J. Jiang, J.-F. Dord, S. Goenezen, and T. G Fisher, "Recent results in nonlinear strain and modulus imaging," *Current medical imaging reviews*, vol. 7, no. 4, pp. 313–327, 2011.

[19] X. Pan, K. Liu, J. Shao, J. Gao, L. Huang, J. Bai, and J. Luo, "Performance comparison of rigid and affine models for motion estimation using ultrasound radio-frequency signals," *IEEE transactions on ultrasonics, ferroelectrics, and frequency control*, vol. 62, no. 11, pp. 1928–1943, 2015.

[20] R. Zahiri-Azar and S. E. Salcudean, "Motion estimation in ultrasound images using time domain cross correlation with prior estimates," *IEEE Transactions on Biomedical Engineering*, vol. 53, no. 10, pp. 1990–2000, 2006.

[21] H. Rivaz, E. Boctor, P. Foroughi, R. Zellars, G. Fichtinger, and G. Hager, "Ultrasound elastography: a dynamic programming approach," *Medical Imaging, IEEE Transactions on*, vol. 27, no. 10, pp. 1373–1377, 2008.

[22] H. Rivaz, E. M. Boctor, M. A. Choti, and G. D. Hager, "Ultrasound elastography using multiple images," *Medical image analysis*, vol. 18, no. 2, pp. 314–329, 2014.

[23] J. Jiang and T. J. Hall, "A generalized speckle tracking algorithm for ultrasonic strain imaging using dynamic programming," *Ultrasound in medicine & biology*, vol. 35, no. 11, pp. 1863–1879, 2009.

[24] S. S. Furuie and F. M. Cardoso, "Estimation of deformations in ultrasound images using dynamic programming." in *Image Processing: Algorithms and Systems/Parallel Processing for Imaging Applications*, 2012, p. 82951K.

[25] M. Omidyeganeh, Y. Xiao, M. O. Ahmad, and H. Rivaz, "Estimation of strain elastography from ultrasound radio-frequency data by utilizing analytic gradient of the similarity metric," *IEEE Transactions on Medical Imaging*, vol. 36, no. 6, pp. 1347–1358, June 2017.

[26] X. Pan, J. Gao, S. Tao, K. Liu, J. Bai, and J. Luo, "A two-step optical flow method for strain estimation in elastography: Simulation and phantom study," *Ultrasonics*, vol. 54, no. 4, pp. 990–996, 2014.

[27] M. A. Hussain, E. M. A. Anas, S. K. Alam, S. Y. Lee, and M. K. Hasan, "Direct and gradient-based average strain estimation by using weighted nearest neighbor cross-correlation peaks," *IEEE transactions on ultrasonics, ferroelectrics, and frequency control*, vol. 59, no. 8, pp. 1713–1728, 2012.

[28] T. Varghese, E. Konofagou, J. Ophir, S. Alam, and M. Bilgen, "Direct strain estimation in elastography using spectral cross-correlation," *Ultrasound in medicine & biology*, vol. 26, no. 9, pp. 1525–1537, 2000.

[29] S. K. Alam, F. L. Lizzi, T. Varghese, E. J. Feleppa, and S. Ramachandran, "Adaptive spectral strain estimators for elastography," *Ultrasonic imaging*, vol. 26, no. 3, pp. 131–149, 2004.

[30] U. Bae and Y. Kim, "Direct phase-based strain estimator for ultrasound tissue elasticity imaging," in *Engineering in Medicine and Biology Society, 2004. IEMBS'04. 26th Annual International Conference of the IEEE*, vol. 1. IEEE, 2004, pp. 1345–1348.

[31] S. R. Ara, F. Mohsin, F. Alam, S. A. Rupa, S. Y. Lee, M. K. Hasan, and R. Awwal, "Phase-based direct average strain estimation for elastography," *IEEE transactions on ultrasonics, ferroelectrics, and frequency control*, vol. 60, no. 11, pp. 2266–2283, 2013.

[32] H. Khodadadi, A. G. Aghdam, and H. Rivaz, "Edge-preserving ultrasonic strain imaging with uniform precision," in *2015 37th Annual International Conference of the IEEE Engineering in Medicine and Biology Society (EMBC)*, Aug 2015, pp. 3835–3838.

[33] M. Khosravi, H. Khodadadi, H. Rivaz, and A. G. Aghdam, "Cooperative receding horizon control of double integrator vehicles for multi-target interception," in *2016 American Control Conference (ACC)*, July 2016, pp. 5525–5530.

[34] M. Khosravi, H. Khodadadi, A. G. Aghdam, and H. Rivaz, "Maximum reward collection problem: A cooperative receding horizon approach for dynamic clustering," in *Proceedings of the 2015 Conference on Research in Adaptive and Convergent Systems*, ser. RACS. New York, NY, USA: ACM, 2015, pp. 38–43. [Online]. Available: http://doi.acm.org/10.1145/2811411.2811550

[35] M. Khosravi, H. Khodadadi, H. Rivaz, and A. G. Aghdam, "Cooperative control for multi-target interception with sensing and communication limitations: A game-theoretic approach," in *2015 54th IEEE Conference on Decision and Control (CDC)*, Dec 2015, pp. 1048–1053.

[36] M. Khosravi, H. Khodadadi, A. G. Aghdam, and H. Rivaz, "A cooperative receding horizon controller for multi-target interception with obstacle avoidance," in *2016 IEEE 55th Conference on Decision and Control (CDC)*, Dec 2016, pp. 93–98.

[37] H. Khodadadi, A. G. Aghdam, and H. Rivaz, "Ultrasound elastography: Direct strain estimation," *Medical Imaging, IEEE Transactions on*, vol. submitted, 2017.

[38] F. Kallel and J. Ophir, "A least-squares strain estimator for elastography," *Ultrasonic imaging*, vol. 19, no. 3, pp. 195–208, 1997.

[39] G. Treece, J. Lindop, A. Gee, and R. Prager, "Uniform precision ultrasound strain imaging," *IEEE Trans. Ultrason. Ferroelectr. Freq. Control*, vol. 56, no. 11, pp. 2420–2436, 2009.

[40] C. Tomasi and R. Manduchi, "Bilateral filtering for gray and color images," in *Computer Vision, 1998. Sixth International Conference on.* IEEE, 1998, pp. 839–846.

[41] G. Treece, J. Lindop, L. Chen, J. Housden, R. Prager, and A. Gee, "Real-time quasi-static ultrasound elastography," *Interface focus*, p. rsfs20110011, 2011.

[42] V. Aurich and J. Weule, "Non-linear gaussian filters performing edge preserving diffusion," in *Mustererkennung 1995*, ser. Informatik aktuell, G. Sagerer, S. Posch, and F. Kummert, Eds. Springer Berlin Heidelberg, 1995, pp. 538–545.

[43] F. Durand and J. Dorsey, "Fast bilateral filtering for the display of high-dynamic-range images," *ACM transactions on graphics (TOG)*, vol. 21, no. 3, pp. 257–266, 2002.

[44] J. E. Lindop, G. M. Treece, A. H. Gee, and R. W. Prager, "Dynamic Resolution Selection in Ultrasonic Strain Imaging," *Ultrasound in Medicine and Biology*, vol. 34, no. 5, pp. 809–823, May 2008.

[45] A. Viterbi, "Error bounds for convolutional codes and an asymptotically optimum decoding algorithm," *IEEE transactions on Information Theory*, vol. 13, no. 2, pp. 260–269, 1967.

[46] R. Bellman, "The theory of dynamic programming," *Bull. Amer. Math. Soc.*, vol. 60, no. 6, pp. 503–515, 11 1954. [Online]. Available: http://projecteuclid.org/euclid.bams/1183519147

[47] P. J. Huber, "Robust statistics. 1981."

[48] J. A. Jensen, "Field: A program for simulating ultrasound systems," in *10TH NORDICBALTIC CONFERENCE ON BIOMEDICAL IMAGING, VOL. 4, SUPPLEMENT 1, PART 1: 351–353.* Citeseer, 1996.

[49] J. Liu, C. K. Abbey, and M. F. Insana, "Linear approach to axial resolution in elasticity imaging," *IEEE transactions on ultrasonics, ferroelectrics, and frequency control*, vol. 51, no. 6, pp. 716–725, 2004.

[50] R. Padgett and C. Kotre, "Assessment of the effects of pixel loss on image quality in direct digital radiography," *Physics in medicine and biology*, vol. 49, no. 6, p. 977, 2004.

[51] M. M. Doyley, Q. Feng, J. B. Weaver, and K. D. Paulsen, "Performance analysis of steady-state harmonic elastography," *Physics in Medicine and Biology*, vol. 52, no. 10, p. 2657, 2007.